The Water Table Model (WTM) v2.0.1: Coupled groundwater and dynamic lake modelling

Kerry L Callaghan[1,2,3], Andrew D Wickert[2,4,5], Richard Barnes[6], and Jacqueline Austermann[3]

[1]Department of Earth & Environmental Sciences, University of Illinois, Chicago, USA
[2]Department of Earth & Environmental Sciences, University of Minnesota, Minneapolis, USA
[3]Lamont–Doherty Earth Observatory, Columbia University, New York, USA
[4]Saint Anthony Falls Laboratory, University of Minnesota, Minneapolis, USA
[5]Deutsches GeoForschungsZentrum (GFZ), Potsdam, Germany
[6]Lawrence Berkeley National Lab, Berkeley, USA

Correspondence: Kerry L Callaghan (kerryc@uic.edu)

Abstract. Ice-free land comprises 26% of Earth's surface and holds liquid waters that delineate ecosystems, affect global geochemical cycling, and modulate sea level. However, we currently lack capacity to simulate and predict these terrestrial water changes over the full range of relevant spatial (watershed to global) and temporal (monthly to millennial) scales. To address this gap in knowledge, we present the Water Table Model (WTM), which comprises coupled components to compute

5 dynamic lake and groundwater levels. The groundwater component solves the 2D horizontal groundwater-flow equation by using non-linear equation solvers in the C++ PETSc library. The dynamic lakes component makes use of the Fill-Spill-Merge (FSM) algorithm to move surface water into lakes, where it may evaporate or affect groundwater flow. To demonstrate the continental scale capabilities of the WTM, we simulate steady-state climate-driven present-day and Last Glacial Maximum (LGM: 21,000 calendar years before present) water table for the North American continent. At the LGM, North America stored

10 6.0 cm sea-level equivalent (SLE) more water in lakes and groundwater than in the climate-driven present-day scenario. We then advance the simulation transiently from 21–16 ka, in which lake volume remains approximately constant but groundwater storage drops by 4.5 cm SLE due to reduced precipitation. Open-source code for the WTM is available on Github and Zenodo.

1 Introduction

Over decades to millennia, global climate and hydrological systems jointly modulate the terrestrial water table (Fig. 1). The

15 water table, defined as the top of water-saturated conditions, controls both groundwater and lake-water storage volumes (Fan et al., 2007, 2013). The volume of stored water changes through time with water-table elevation as a result of seasonality, human impacts, or longer-term changes in climate and topography. These changes in lake and/or groundwater systems significantly impact the hydrological cycle on a global scale (Ni et al., 2018; Syed et al., 2008).

The upper 2 km of continental crust holds an estimated 22.6 million km^3 of groundwater (Gleeson et al., 2016). This ground-

20 water provides baseflow to rivers and lakes, defines wetland locations (Fan et al., 2013; Zhu and Gong, 2014), and provides a large store of freshwater for human use (Wada, 2016). It also changes over time, with impacts on ecosystems (Amanambu

et al., 2020; Cuthbert et al., 2019b; Hu et al., 2017), geochemical cycling (Dean et al., 2018; Ringeval et al., 2010; Zhang et al., 2023b), and sea level (Konikow, 2011; Pokhrel et al., 2012; Sun et al., 2022; Wada et al., 2012). Meanwhile, although lakes cover only about 3.7% of the Earth's ice-free land surface (Verpoorter et al., 2014), they are numerous: Verpoorter et al. (2014)

25 recorded over 100 million lakes in their inventory. The total volume of the world's lakes is about 181,900 km^3 (Messager et al., 2016). This lake-water storage impacts hydrologic connectivity (Callaghan and Wickert, 2019), and therefore also sediment and contaminant transport. Surface-water elevation also influences groundwater head, and may exert a stronger control on head in gradient-based groundwater models than other factors, including recharge and hydraulic conductivity (Reinecke et al., 2019a). The extent of these water stores highlights the importance of understanding how they change in the long term.

30 High-performance computing and efficient algorithm design have enabled continental-scale modelling of modern-day groundwater (Fan et al., 2013; Maxwell et al., 2015) and streamflow (Döll et al., 2009; NOAA, 2016). However, we lack models that are capable of global-scale transient simulations lasting decades or longer. These time scales are highly relevant for our understanding of the impacts of changing sea level and climate on groundwater stores, and are of particular importance for understanding changes to the hydrological system over human lifetimes. Existing models that include simulation of groundwa-

35 ter at large spatial scales either allow for steady-state simulation (Fan et al., 2013; Maxwell et al., 2015) or transient simulations at timescales from hours to a few years (Maxwell et al., 2015; Kollet, 2009; O'Neill et al., 2021). Some hydrologic projections over longer time periods (decades) do exist (Döll et al., 2020; Märker and Flörke, 2003), but these do not explicitly simulate the groundwater table.

Built-in static assumptions and/or equilibrium approaches prevent existing models from adequately considering the possibly

40 of dramatic long-term changes to lake volume, especially when those involve changes in lake extent. Various land-surface models (Decharme et al., 2019; Koirala et al., 2014; Lawrence et al., 2019; Wiltshire et al., 2020; Yokohata et al., 2020; Zeng et al., 2002, e.g.) provide complex depictions of surface and sub-surface hydrology. Some include lake components that influence local climate (Oleson et al., 2010), but they do not incorporate dynamic changes in lake-water storage or lake surface area through time. For example, Müller Schmied et al. (2021) comprehensively simulated surface hydrology, including

45 dynamics of lake and wetland storage (Döll et al., 2020), but relied on static mapped extents of lakes and wetlands. Many of the aforementioned models also have substantial data input and calibration requirements, complicating assessment of long-term changes in the water table, which necessarily integrate across times for which requisite data are scarce.

To address the challenge of long-term transient simulation of the water table, we present the Water Table Model (WTM). The WTM couples groundwater (Section 3) and lake-water (Section 4) levels and flow to simulate water-table elevation relative to

50 the land surface across spatial scales from local catchments to the globe and over time scales from months to thousands of years and beyond. By explicitly acknowledging the link between surface-water elevation and groundwater head, the WTM moves beyond the common – but artificial – model truncation at the land surface, and instead solves the dynamically linked surface- and groundwater system (Reinecke et al., 2019a, b). Input data to the WTM are commonly available for both the present day and recent geological past, and are described in Appendix A1.

55 We designed the WTM with the following goals and philosophies: (1) Simplicity – the focus of the model is on the simulation of the water table alone. Vadose zone processes, climate, and streamflow are not directly simulated. (2) Computational

efficiency – this allows the WTM to be run across hundreds of millions of cells for thousands of years. (3) Open-source model code – the source code for the WTM is available on GitHub (https://github.com/KCallaghan/WTM/, v2.0.1) and Zenodo (https://doi.org/10.5281/zenodo.10611076, v2.0.1) for other researchers to use and peruse. (4) Dynamic lakes – lake locations

60 are not predefined and evolve alongside the rest of the water table. (5) Broad applicability – the WTM can be used across a broad range of spatial scales, from catchment to global, and can produce both transient and steady-state water-table outputs.

The objective of this paper is to fully explain the methodological structure of the WTM and share examples of the results it can produce. In Sections 2 to 5 and the related Appendices A to E, we describe in full this methodology. In Section 6, we provide results from a steady-state climate-driven present-day WTM simulation for North America. Here, the climate-driven

65 present-day water table is impacted by recent, human-influenced climate and topography, but other anthropogenic impacts such as water extraction from pumping are not included. We also present a Last Glacial Maximum (LGM) WTM simulation for North America, as well as a series of transient simulations for this region from 21,000 to 16,000 calendar years before present.
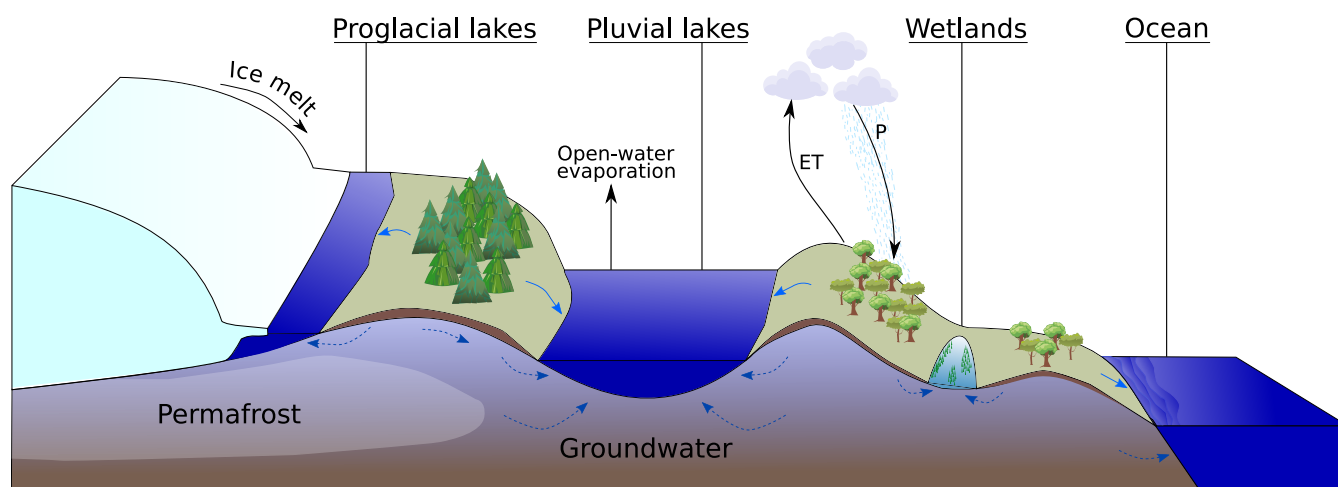
Figure 1. The water table, incorporating groundwater and lake surfaces, is an integral part of the global hydrologic system, interacting with all of the other major hydrologic stores, including ice, ocean, and atmosphere. In this figure, solid blue arrows indicate direction of surface-water flow, and dotted darker blue arrows indicate direction of groundwater flow.

2   Model summary

70 The WTM (Callaghan, 2023) simulates water-table elevation relative to the land surface (here referred to as relative water table elevation, or z_{wr}), inclusive of both groundwater and dynamically changing lake surfaces. Water table is controlled by sea level, topography, and water inputs (precipitation, icemelt) and outputs (evapotranspiration, open-water evaporation). Groundwater flow is dependent on local hydraulic conductivity, discussed further in Section 3.2, and slows in permafrost regions.

Within the WTM, separate model components for simulation of groundwater (Section 3) and dynamic lakes (Section 4) are run sequentially in a repeated cycle to permit feedbacks between ground- and surface water in the terrestrial hydrological system (see Fig. 2). Both groundwater and dynamic lake components use the same sets of input data and modify the same water table array to produce one final water table, with groundwater represented as negative z_{wr} values and lakes as positive z_{wr} values. Any water that exfiltrates during the groundwater step is moved downslope and into lakes or the ocean during the surface-water step; conversely, seepage from lakes may occur during the surface-water step and lake-water is included in the hydraulic head field used to calculate groundwater movement.

The WTM is implemented in C++. The code can be acquired from Github (https://github.com/KCallaghan/WTM, last access 30 April 2024) and Zenodo (v2.0.1, https://zenodo.org/records/10611076).

The WTM captures broad natural patterns in water table elevations. Its simplified treatment of groundwater flow makes it most appropriate for large spatial scales, from continent-spanning catchments to the globe, and its assumption that surface water always completes its travel to depressions or to the ocean makes the WTM most appropriate for long temporal scales, from months to millennia. In addition to transient simulations, the WTM can also be used to simulate a steady-state water table for any given set of conditions. For steady-state model runs, the user must run the model for long enough to allow the water table to equilibrate to the given topography and climate. If users wish to monitor change in the water table, values indicating the total change in the array are saved to a text file, and the full water table is saved at user-defined intervals. For transient runs, the user will simply select the amount of time for which to run the simulation, and provide input data at the start and end points of the simulation. The input data required by the WTM are listed in Appendix A1. As an output, the WTM returns a 2D array z_{wr}, which equals the water-table elevation minus the land-surface elevation (positive values indicate exposed surface water while negative values indicate groundwater).

Figure A1 demonstrates the steps followed within the coupled model. Note that the only practical difference between a steady-state and a transient model run is that the transient model run includes the possibility for topographic and climatic change, which requires that input files be modified and the depression hierachy be recalculated during the course of the simulation.

3 The Groundwater Component

3.1 Computing the groundwater table

We compute the groundwater table at each time step using the 2D horizontal groundwater flow equation (Equation 1) for saturated groundwater flow in an unconfined, heterogeneous aquifer (Freeze and Cherry, 1979). This method invokes the Dupuit–Forchheimer approximation, which posits the assumptions that flowlines are horizontal and that the hydraulic gradient is equal to the slope of the water table and does not vary with depth below the water table.

$$S_y \frac{\partial h}{\partial t} = \frac{\partial}{\partial x}\left(T\frac{\partial h}{\partial x}\right) + \frac{\partial}{\partial y}\left(T\frac{\partial h}{\partial y}\right) + R. \tag{1}$$
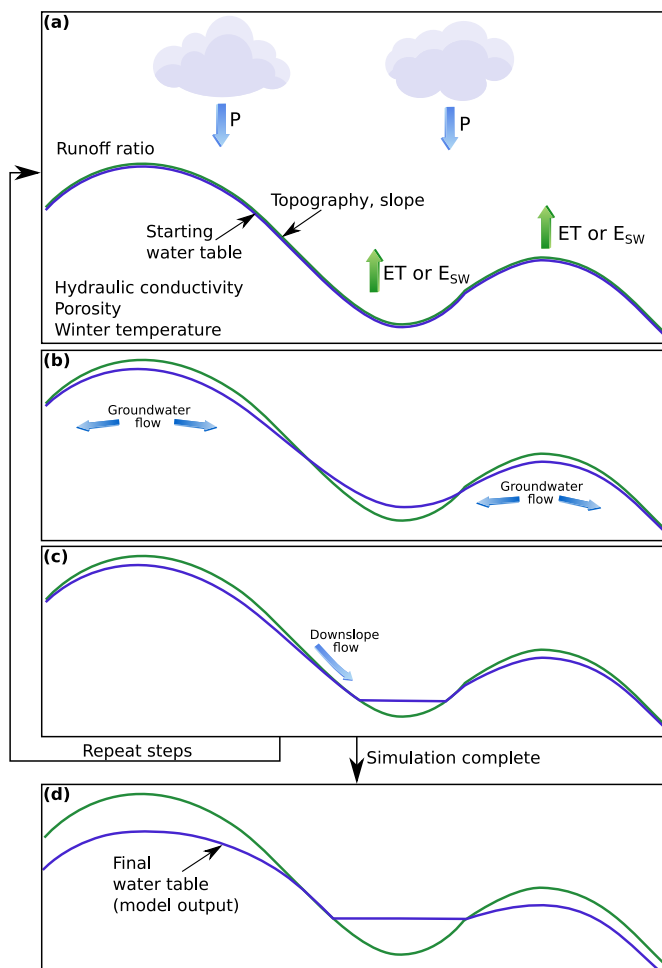
Figure 2. A schematic of the WTM. **(a)** A cross section across a hypothetical portion of a landscape, including hillslopes and a depression that may hold a lake. Inputs to the WTM include precipitation (P), evapotranspiration (ET), surface-water evaporation (E_{SW}, used in the place of ET when lakes are present), topography, topographic slope, runoff ratio, hydraulic conductivity, porosity, and winter temperature. A starting water table may be provided or, for steady-state runs, the water table will be initiated at the land surface. **(b)** The groundwater component executes and groundwater flow modifies the water table. Here, the water table is deeper below the hilltops and exfiltration has occurred on hillsides. **(c)** FSM (the dynamic lake component) has executed. Surface water is now distributed from hillslopes into lakes at the bottom of depressions. Steps (a) to (c) repeat until the user-defined amount of time steps have been completed. **(d)** The simulation is complete and the resulting water table is saved to a file.

105 Here we solve for h, the groundwater head. T is the transmissivity (depth-integrated hydraulic conductivity, see Section 3.2). t is time. x and y are the two dimensions of groundwater movement. R is recharge; details on how values for R are selected are given in Section 3.3. S_y is specific yield, here approximated as being equal to porosity and provided as input data by the user.

To solve Equation 1, we use the Scalable Nonlinear Equations Solvers (SNES) component of PETSc (Portable, Extensible Toolkit for Scientific Computation) (Balay et al., 1997, 2022a, b) in C++. Full details on the discretisation and implementation

110 of this equation are given in Appendix B.

In the simulations included within this paper, we use the Anderson (1965) Mixing method (selectable at runtime), which iteratively solves nonlinear equations, to compute groundwater head, h, at regular time intervals. Converting h to the relative water-table elevation, z_{wr}, is trivial: $z_{wr} = z + h$, where z is the elevation of the land surface.

3.2 Transmissivity

115 Transmissivity (T) — the depth-integrated hydraulic conductivity from $-\infty$ to z_{wr} — is needed to solve for groundwater flow (see Appendix B). To obtain T, we require knowledge of hydraulic conductivity values through the entire depth of the aquifer. Data on variability of hydraulic conductivity with depth are not available at the spatial scales we assess here, so we follow the common assumption that this value decreases exponentially with depth (Ameli et al., 2016; Cardenas and Jiang, 2010; Fan et al., 2013). Users provide a single near-surface hydraulic conductivity value in each cell of the domain, which is used from

120 the land surface to a depth of $1.5\,\mathrm{m}$ because global soil datasets are representative of the conditions until approximately this depth. We term this $K_{1.5}$. Beyond depths of $1.5\,\mathrm{m}$, hydraulic conductivity decays exponentially from this near-surface value.

We specify the rate of this exponential decay using an e-folding depth (f_d). Local terrain slope is used as a modifier: steeper slopes support less sediment and so hydraulic conductivity decays more rapidly. A temperature-dependent modifier (T_f) further decreases the e-folding depth at locations where seasonal frost or permafrost occur:

125
$$f_d = f \times T_f, \tag{2}$$

where f is the slope-dependent term, defined as:

$$f = \max\left(f_{\min}, \frac{a}{1+bS}\right), \tag{3}$$

where S is the terrain slope; and a, b, and $f_{\min}$ are user-selected calibration constants.

T_f is incorporated into the e-folding depth following the method and temperature ranges used by Fan et al. (2013). When the

130 average winter temperature drops below $-5°\,C$, we assume that seasonal frost inhibits groundwater flow. When average winter temperatures fall below $-14°\,C$, we assume that groundwater flow is affected by permafrost. This limits lateral drainage, reducing the effective hydraulic conductivity (Fan and Miguez-Macho, 2011). We define T_f as:

$$T_f = \begin{cases} 1, & \text{if } (T_C > -5°C) \\ 1.5 + 0.1T_C, & \text{if } (-14°C < T_C < -5°C) \\ \max(0.17 + 0.005T_C, 0.05), & \text{if } (T_C < -14°C), \end{cases} \tag{4}$$

where T_C is the temperature in degrees Celsius.

135   With this hydraulic conductivity structure in hand, we calculate transmissivity. We consider three possible cases:

1. The water table lies below 1.5 m depth, where the exponential decay of hydraulic conductivity comes into play. We must use the f_d values computed earlier.

2. The water table lies in the shallow subsurface, above 1.5 m depth, where the unmodified hydraulic conductivity from our input data are representative of conditions at the water table.

140   **3.** The water table lies above the land surface. In this case, hydraulic conductivity is calculated at the level of the land surface (i.e. it is identical to that for a fully saturated substrate). The dynamic lake component (Section 4) later moves the surface water into depressions or out of the domain as appropriate.

Based on these three cases for hydraulic conductivity, we follow the methods used by Fan et al. (2013) to calculate transmissivity as:

$$
145 \quad T = \begin{cases} f_d \times K_{1.5} \times \exp\left(\frac{z_{wr}+1.5}{f_d}\right), & \text{if } (z_{wr} < -1.5\,\text{m}) \quad \leftarrow \text{deep subsurface} \\ K_{1.5} \times (z_{wr} + 1.5 + f_d), & \text{if } (-1.5\,\text{m} \le z_{wr} \le 0\,\text{m}) \quad \leftarrow \text{shallow subsurface} \\ K_{1.5} \times (0 + 1.5 + f_d), & \text{if } (0\,\text{m} < z_{wr}) \quad \leftarrow \text{above surface,} \end{cases} \tag{5}
$$

where T is the transmissivity, f_d is e-folding depth (Equation 2), $K_{1.5}$ is the shallow sub-surface horizontal hydraulic conductivity (assumed valid to a depth of 1.5 m), and z_{wr} is the relative water-table elevation. See Fan et al. (2013) for more information on the derivation of these formulæ.

3.3 Recharge and evaporation

150   We use the climatic water input (W_{in}, including precipitation and any other incoming water, such as icemelt), overland evapotranspiration (ET), and open-water evaporation (E_{SW}) input arrays (see Appendix A1 for a full list of all required input arrays) along with the optional runoff ratio array (r_r) to determine how much water is available to recharge the groundwater table and how much surface water will evaporate.

When surface water is present, evaporation rates typically increase. Physically, this is because actual evaporation is able
155   to equal potential evaporation. Both physically and algorithmically, this typically acts as a feedback that slows runaway lake growth by decreasing the catchment-wide water balance as the lake surface area increases. If lakewater is present in a cell, then sufficient evaporation can subtract water from the cell; in cells that do not contain lakes, sufficient evapotranspiration can mean that there is no water available to add to groundwater, but the earth surface shields the groundwater itself from evaporation. To account for the changes in evaporation dependant on the presence of surface water, the WTM recalculates the total water
160   input to each cell (Equation 6) at the beginning of each groundwater–surface-water model cycle. This total water input (W_{tot}) is given by:

$$
W_{tot} = \begin{cases} \max(W_{in} - ET, 0) & \text{if } z_{wr} \le 0 \quad \leftarrow \text{subsurface} \\ W_{in} - E_{SW} & \text{if } z_{wr} > 0 \quad \leftarrow \text{above surface,} \end{cases} \tag{6}
$$

Optionally, a user can provide a spatially distributed runoff ratio, r_r, which sets the proportion of incoming water that runs off over the land surface rather than infiltrating into the subsurface. This runoff is routed overland via the dynamic lake component of the model, discussed in Section 4, and the remaining water is treated as local recharge and applied to the water table. If unassigned, $r_r = 0$ by default.

The amount of runoff, r, in each cell where $W_{tot} > 0$ is:

$$r = r_r W_{tot}. \tag{7}$$

As its complement, recharge is defined as:

$$R = W_{tot} - r. \tag{8}$$

Equation 8 indicates that the WTM neglects unsaturated-zone processes. We made this design decision for three reasons. First, we sought to maintain the simplicity of the modelling framework in order to understand and interpret its results. Second, the time-scale of unsaturated-zone processes becomes increasingly negligible with longer-term simulations (Sousa et al., 2013), and so we choose to neglect these in the multi-millennial-scale simulations we include here. Third and most importantly, simulating the unsaturated zone is computationally expensive (Maxwell et al., 2015) and prohibits the multi-millennial continental scale model runs that we show in this work.

4 The dynamic lake component

The dynamic lake component uses a parsimonious graph-based approach to move surface water into depressions and to compute surface-water storage within these depressions. Depressions are defined as inwardly draining regions within the topography, where water would naturally pool without being able to flow away. The dynamic lake component proceeds in two steps: (1) It computes a *depression hierarchy* (Barnes and Callaghan, 2020) based on an input digital elevation model (DEM), and (2) it uses the Fill–Spill–Merge method, modified to include lake seepage and, optionally, infiltration, to rapidly allocate runoff to these depressions (Barnes et al., 2021) and to calculate the resulting depth of surface water in all of the depressions.

4.1 The depression hierarchy

Understanding the topological and geographical relationships between depressions in the landscape allows us to more rapidly calculate how these depressions will trap and store water. An unfilled depression will retain water that flows into it, while a depression that is already filled with water will overflow either to another depression or to the ocean. The depression-hierarchy algorithm builds the *depression hierarchy* data structure (Barnes and Callaghan, 2019) by analysing the input topography to determine the locations of internally drained depressions and their catchments. We use this data structure (see Barnes and Callaghan, 2019, 2020, for a full description) to compute surface-water flow using Fill–Spill–Merge, discussed in Section 4.2. The depression hierarchy is scale independent, though the accuracy of the computed depression network depends on the quality and resolution of the input DEM.

In this work, we have modified the original depression-hierarchy code described by Barnes et al. (2020) in two critical ways. First, we relaxed the assumption of uniform grid-cell size. Second, we now account for groundwater storage in each cell.

4.1.1 Latitude-dependent variable cell areas

When performing computations using geospatial data represented on a latitude-longitude grid, cells at higher latitudes will have smaller areas than cells at lower latitudes due to the roughly spherical shape of the Earth. Therefore, we generalise the code to allow for latitude-dependent variable cell sizes (Callaghan, 2023). This modification is crucial for our ability to conserve water volume as water moves from cell to cell.

4.1.2 Groundwater storage

Here, we modify the depression hierarchy to record the volume available for water storage below the land surface in a given depression (i.e., the groundwater space below cells that may receive an influx of surface water). This allows the algorithm to more accurately assess the total capacity for water storage in each depression. This change was necessary for use in the WTM, because we consider both surface and groundwater. When the water table is below the land surface, we assume that the ground will become saturated before surface water begins to fill the depression.

4.2 Fill–Spill–Merge

The WTM computes lake levels using the Fill–Spill–Merge (FSM) algorithm (Barnes and Callaghan, 2020; Barnes et al., 2021). FSM rapidly routes surface water downslope into depressions using a depression hierarchy (Section 4.1), Barnes et al. (2020). If a depression has been filled by precipitation or run-off to the point where it can't contain any more water, that depression will spill, sending any additional water to its neighbouring depression. If two neighbouring depressions are both filled, they will merge to form a larger metadepression, which will then continue to fill with water. This process continues until all surface water flows either to a depression or to the ocean. This combination of a depression hierarchy and FSM solves the above flow-routing and water-distribution problem thousands of times faster than previous models (Barnes and Callaghan, 2019; Barnes et al., 2021).

FSM is time-independent, always moving surface water to its final destinations in depressions, the ocean, or out of the model domain within a single time interval. We apply this in the WTM under the assumption that surface water movement is fast in comparison to that of groundwater, and that only equilibrated surface-water results are needed over the time-scales we address using the WTM. Overland flow, including streamflow, is implied through the calculation of flow directions and the final locations of standing water, but is not explicitly modelled. The output of FSM is an array showing the updated z_{wr}, after infiltration has (optionally) occurred and surface water has either flowed into depressions to form lakes or exited the domain.

In this work, we add optional infiltration, discussed in section 4.2.1, to the original FSM algorithm from Barnes et al. (2021). We also implement seepage from lake cells (Section 4.2.2) and allow cell size to vary with latitude (Section 4.2.3).

4.2.1 Infiltration

Here, we add an optional infiltration component to FSM. When the infiltration option is enabled, the FSM algorithm first
225 moves surface water downslope cell-by-cell, using the flow directions generated by the depression hierarchy. As the water
moves downslope, some may infiltrate; the remainder continues along the flowpath until it flows into the ocean, out of the
domain, or into a pit cell (that is, the cell within a depression that has the lowest elevation).

When the infiltration option is disabled, the land surface will be treated as impermeable in order to simulate rapid evacuation
of surface water from each cell via river networks. To speed calculations, the algorithm will skip cell-to-cell water flow and
230 instead will use the depression hierarchy data to move water directly from each surface water-containing cell to the relevant
depression in the hierarchy.

Our method for managing infiltration considers the vertical hydraulic conductivity within the cell, the travel time of water
across the cell, and the amount of unsaturated below-ground space in the cell that can potentially accommodate infiltrating
water. For full details on the method used, see Appendix C. Here, we summarise the amount of infiltration (I) that occurs in a
235 cell with the equation:

$$I = \min\left(-\phi z_{wr} \ , \ I_{\text{pot}}\right), \tag{9}$$

where infiltration is the minimum value of the amount of unsaturated below-ground space, or subsurface porosity (ϕ) multiplied
by negative relative water table elevation ($-z_{wr}$), and the maximum potential infiltration (I_{pot}) that could occur in that cell.
I_{pot} is defined as:

$$
240 \quad I_{\text{pot}} =
\begin{cases}
h_0 & \text{if } h_0^{5/3} \leq \frac{5}{3} \frac{n}{S^{1/2}} k_{\text{sat}} \Delta L \\
k_{\text{sat}} t_I & \text{otherwise,}
\end{cases}
\tag{10}
$$

where h_0 is the initial height of water entering the cell; n is the Gauckler–Manning coefficient, here set to a default value of
$0.05 \, m^{-1/3}s$; S is the slope; k_{sat} is the infiltration rate; and t_I is the transit time of water across the cell.

Use of the infiltration module is only recommended for cases in which the input data have a high enough resolution to
resolve hillslopes and river channels that wholly occupy distinct individual cells. When using coarser resolution input data, a
245 single pixel will contain sections of both river network and hillslope, and the model will not have sufficient information about
the transit routes and times of water across these different zones, themselves determined by drainage density and hillslope
geometry, to realistically simulate infiltration. When input data resolution becomes high enough to differentiate these hillslope
and channel components of the landscape, the infiltration component adds an additional element of realism to the model.

4.2.2 Seepage

250 When a lake is present in a depression, we allow the water column to instantaneously seep into the subsurface until either
(a) the full subsurface is saturated or (b) no surface water remains. The WTM does not simulate any perched water tables; a
lake surface represents the water table with complete saturation up to that elevation.

4.2.3 Variable cell areas

As mentioned in Section 4.1.1, cell areas for unprojected geospatial data can vary dramatically based on latitude. The same
volume of water at two different latitudes would translate to a different thickness of ground- or surface water in a cell. As with
the depression hierarchy, we account for this variable cell area when calculating z_{wr}, allowing us to conserve water volume
within the model.

5 Computational performance

In a scaling test, we found an approximately $\mathcal{O}(n^2)$ scaling between runtime and the number of cells in the domain. Our
test used several square-sized datasets from the GEBCO2020 dataset GEBCO Bathymetric Compilation Group (2020) with
the smallest dataset spanning 54 to 55 °N and 102 to 103 °W and the largest dataset spanning 43 to 73 °N and 74 to 104
°W (northeastern North America). We used uniform values for other input data (precipitation, evapotranspiration, porosity,
hydraulic conductivity, winter temperature). Scaling tests were run on a desktop computer with an Intel(R) Core(TM) i9-10900
CPU @ 2.80GHz processor with 2 threads per core, 10 cores per socket, and 134 GB RAM. For larger datasets, such as those
shown in Section 6 below, high-performance computing (HPC) is recommended.

In this scaling test, the SNES convergence tolerance ($stol$) was set to 10^{-6}f and the Anderson (1965) solver was used (this
solver is recommended for all WTM runs). The majority of the computation time is spent in solving for groundwater flow;
performance metrics for FSM alone are given by Barnes et al. (2021).

The balance between performance and cell count makes it possible to perform simulations at a continental scale with a
30-arcsecond cellsize, as described below in Section 6. Smaller topographic areas could reasonably be simulated with corre-
spondingly finer spatial resolutions.

6 Example: North America

To demonstrate the capabilities of the WTM and benchmark it against both models and data, we have computed the steady-
state water table across North America in the climate-driven present day ($\sim$1958-2018). We do not simulate direct human
interventions (e.g. groundwater pumping or irrigation), but the results inherently incorporate human impacts on climate and
topography through the input data. We include comparisons between these model results and similar calculations – albeit
without dynamic lakes – performed by Fan et al. (2013) and Reinecke et al. (2019b) as well as against groundwater-level (Fan
et al., 2013), wetland (Zhang et al., 2023a), and lake-level (Kourzeneva et al., 2012) observational data. We also include a
simulation of the steady-state water table at the LGM, which is run on a paleotopography that accounts for glacial isostatic
adjustment (GIA) and is forced by past ice sheets (Peltier et al., 2015) and paleoclimate GCM outputs (He, 2011). The resulting
water-table pattern differs significantly from the present-day simulation, including proglacial lakes, pluvial lakes, and changes
in groundwater levels. Finally, we include a simulation of transient water-table change from 21,000 to 16,000 calendar years
before present. This simulation used the equilibrated LGM simulation as an initial condition. Simulated water-table variability

amounted to 4.5 cm sea-level equivalent, demonstrating the dynamic potential of the terrestrial hydrological system on the
285   global water budget.

6.1   Equilibrium run: present day

We used the WTM to simulate the present-day climate-driven water table for the North American continent (Fig. 3) at a spatial
resolution of 30 arcseconds. Details on the input data used are given in Appendix E. The groundwater table was computed in
steps of 1/10 years, with FSM executed once per year.
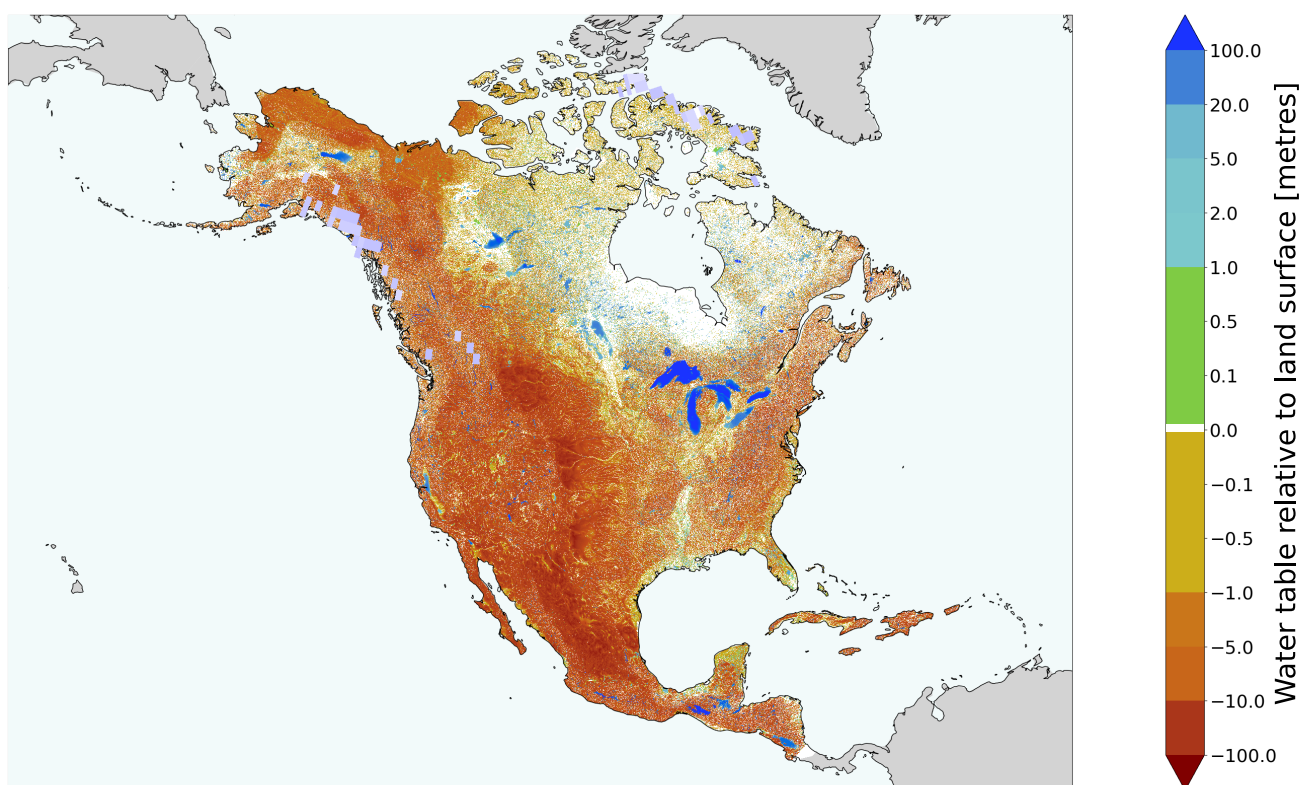
Figure 3. Simulated climate-driven water table for present day North America. Positive values indicate lake depths and negative values
indicate the depth of groundwater tables beneath the land surface. The basemap includes ocean (pale cyan) and land (grey). Continental ice
thickness from ICE-6G (Peltier et al., 2015) varies from blue-grey (thin) to white (thick), with most modern ice being thin.

290   To reach steady-state, we ran this simulation for over 20,000 years. This is significantly longer than the global median
groundwater response time of 5727 years noted by Cuthbert et al. (2019a); furthermore, Cuthbert et al. (2019a) provide a
groundwater response time of 1238 years when excluding hyper-arid regions and note that approximately 25% of Earth's land
surface responds in under 100 years. To confirm whether our simulation had reached a reasonable degree of equilibration, we

computed e-folding response times for the equilibration of our simulated water table for every cell in the domain. We found
295   that the median e-folding response time for our present day WTM simulation was 2792 years.

This simulation captures broad climate-driven patterns in z_{wr} at a continental scale. The drier climate in the west results in deeper water tables while wetter climates in the north and east result in shallower water tables. Variable geology and topography add detail to this overall pattern driven by the climatic gradient.

6.1.1   Comparison to observations

300   Here, we compare our simulation result to observed groundwater-table depths, lake depths, and wetland extents. Together, these observations cover 11.3% of the cells within our North American domain. This coverage comprises 11% groundwater wells, 50% lake cells, and 39% wetlands.

Groundwater-table data come from an extensive archive of water table observations gathered by Fan et al. (2013). We cleaned these data to remove readings where 'nodata' values were provided for either water table or topography, and removed those
305   with negative water-table depths or with depths greater than the maximum well depth for the dataset. After this cleaning, more than 900,000 data points remained. In cases with multiple data points per 30 arcsecond grid cell, we averaged the values, leaving over 500,000 cells containing groundwater observations.

We obtained lake extents and depths from the Kourzeneva et al. (2012) lake-bathymetry dataset. This contains spatially distributed bathymetric data for large lakes and mean depths for thousands of smaller lakes. When depth was unknown, this
310   dataset uses a default value of 10 m.

Wetlands are from the Zhang et al. (2023a) wetland map. We included all wetland classes with the exception of 'permanent water' (i.e. lakes). We assumed that wetlands had a relative water table elevation equal to 0 m, i.e. that the water table was at the land surface.

We compare the WTM results to the observed groundwater, lake, and wetland data in Fig. 4. Because lake and wetland
315   data cover a much larger spatial area than the groundwater data, they appear as higher proportions in these histograms. The histograms also emphasise several issues with the observed dataset: (1) the Kourzeneva et al. (2012) lake dataset provides only mean depths for a majority of the lakes included, resulting in peaks at certain values that are not matched in simulation. Notably, the peak at 10 m depth corresponds to the default depth chosen by Kourzeneva et al. (2012) when lake depth was unknown. (2) Although we assume wetland water tables to represent water tables exactly at the land surface, they may in reality
320   lie above or below it. Our assumption that wetlands have water table equal to the land surface results in a peak in the data at 0 m, while near-zero values remain undersampled. (3) Groundwater wells might not be sampling over the full range of actual groundwater depths, especially in locations with very shallow or very deep water tables (Fan et al., 2013). (4) Groundwater pumping may occur at or near some wells, depressing the observed water table. These issues may account for a substantial amount of the discrepancy seen between simulation and observations. Improvements in observed data in the future will enable
325   us to better test simulated results. Improvements in model inputs as input gridded data products, including observations and simulations of topography and climate, improve should also increase the accuracy of WTM results in the future.

Scatter plots show some variation between simulated and observed water table on a cell-by-cell basis (Fig. 5), though it is notable that many simulated cells match the observations. The many potential reasons for any discrepancies include seasonal variations in observed data; water table not being at steady-state in the real world; and differences in water table and topography

330   within the 30 arcsecond cell size. On the other hand, there is a very close agreement between modelled and observed hydraulic head, indicating that hydraulic head is likely dominated by the topographic signal.
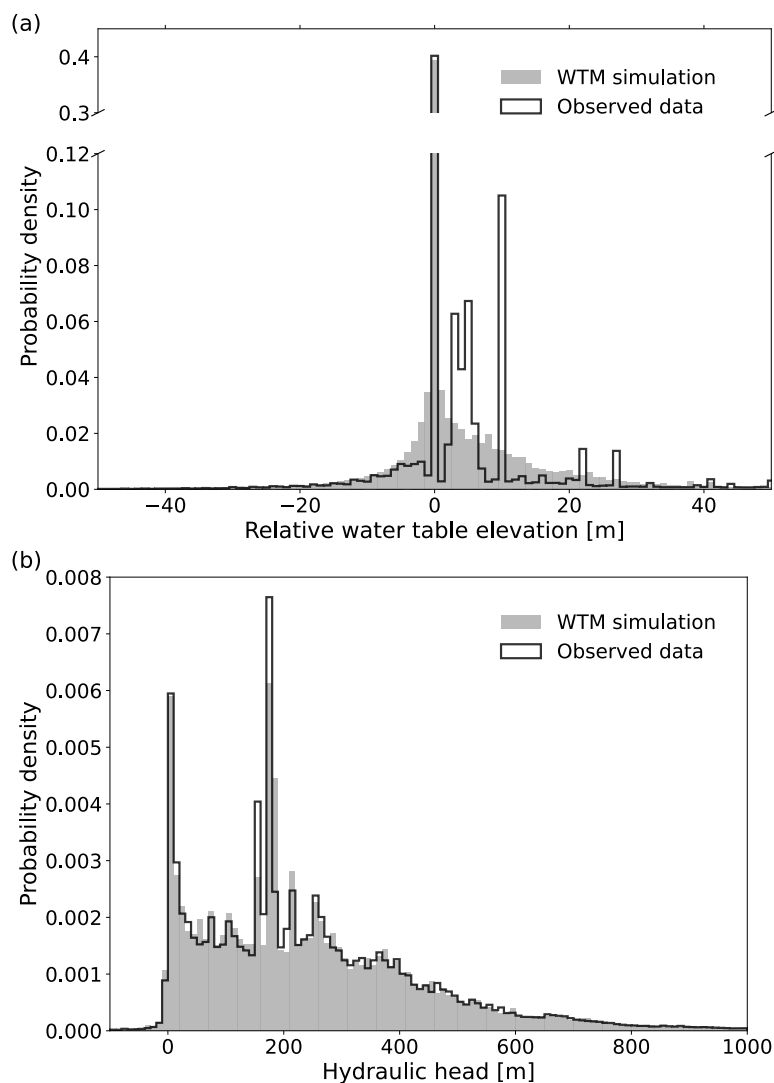
Figure 4. Simulated versus observed present day climate-driven water table in North America. (a) Relative water-table elevation; **(b)** hydraulic head. Observations include lake, wetland, and groundwater-well data from Kourzeneva et al. (2012), Zhang et al. (2023a), and Fan et al. (2013), respectively. A small proportion of both observations and simulated relative water-table elevations and heads lie outside the x-axis limits.
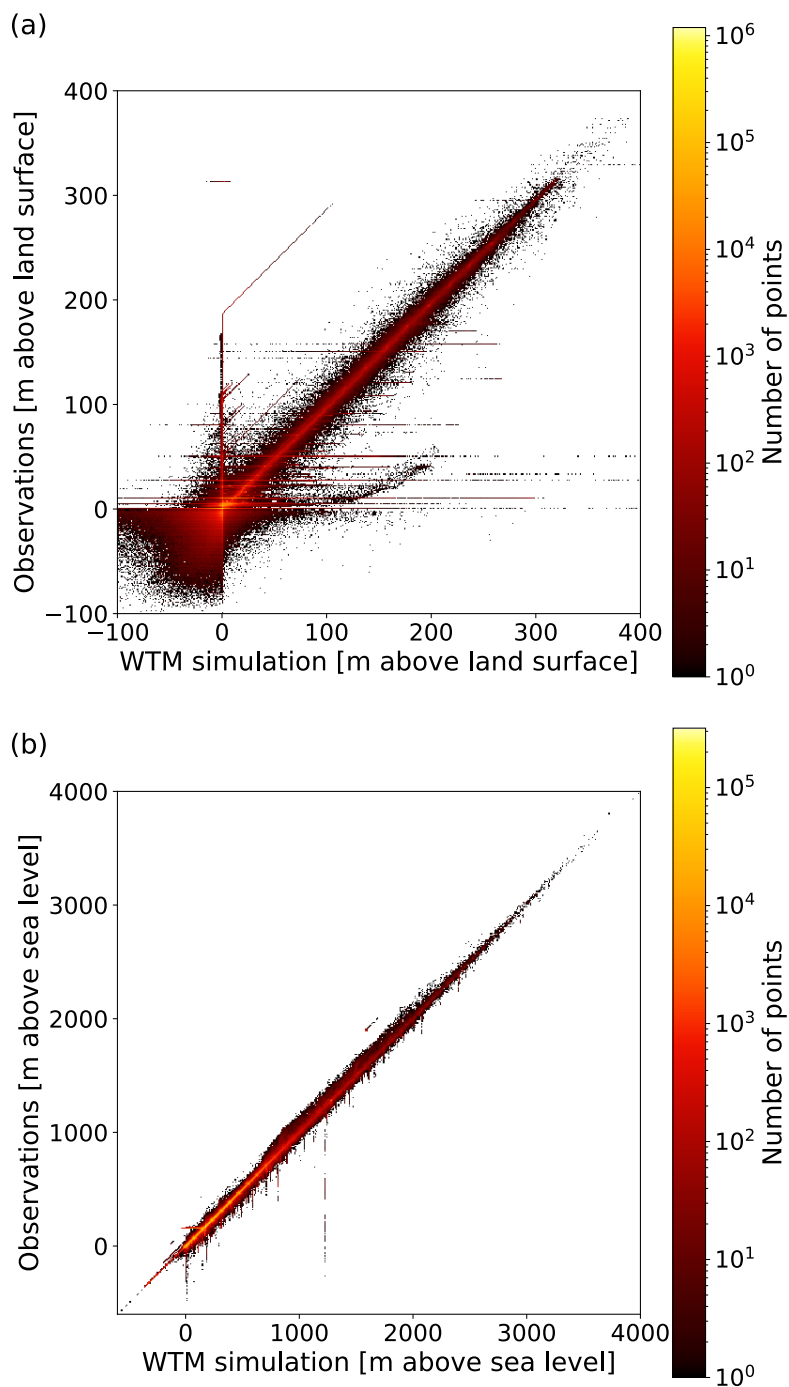
Figure 5. Observations vs. WTM simulation results. (a) Relative water table elevation; **(b)** Hydraulic head. These comparisons include only those model cells that contain observations.

6.1.2 Comparison to other simulations

Here, we compare results from the WTM's present day simulation to results from two steady-state simulations of present-day climate-driven groundwater table for North America: Fan et al. (2013) and Reinecke et al. (2019b) (G3M).

335 Fan et al. (2013) completed their simulation at a spatial resolution of 30 arcseconds. They did not include lakewater, instead assuming that all water above the land surface would either evaporate or run off. Comparison to the WTM is shown in Fig. 6(a) and (b). G3M (Reinecke et al., 2019b) had a coarser spatial resolution of 5 arcminutes, meaning that 100 cells from our WTM run fit within each G3M cell. Like WTM, G3M focuses on simplicity and drives groundwater flow with hydraulic head. However, G3M treats surface water as a static boundary condition with prescribed proportions of lake and wetland extent in

340 each model cell. Positive water-table elevation values in the G3M outputs do not represent actual lake depths, and surface water may be exported to the static lake and wetland classes (not included within their results). Comparison to the WTM simulation is shown in Fig. 6(c) and (d).

The inclusion of dynamic lakes in the WTM simulation accounts for a large proportion of the difference in relative water-table elevation distribution between this and the other two simulations. We note that because of the inclusion of lake surfaces in

345 our work, we also expect water tables in areas surrounding lakes to be higher than those simulated by Fan et al. (2013) or G3M (Reinecke et al., 2019b). The WTM has, as expected, positive relative water-table elevations (indicative of lake depths) and a larger proportion of cells in the -0.5 m to 0.5 m range (incorporating shallow groundwater) than both of the other simulations. The Fan et al. (2013) and G3M (Reinecke et al., 2019b) simulations make up these proportions in slightly deeper groundwater categories. The significantly lower proportion of cells in the -0.5 m to 0.5 m range in the G3M simulation may be a result of

350 export of this water to their wetland and lake classes, which were not provided in their results. Head values, which are largely dominated by topography, match well across simulations. The WTM output contains fewer low-head values than either of the other simulations. This may result from the inclusion of lake surfaces in the WTM, which increases average head.

6.2 Equilibrium run: North America at the Last Glacial Maximum

21,000 calendar years before present (21 ka), at the LGM, the world was on the brink of experiencing thousands of years of

355 dramatic sea level rise, ice retreat, and changing climate. Lower sea level, greater ice extent, and different climate at the LGM all mean that water table at this time also differed from today's. We used the WTM to simulate steady-state water table for the North American continent at 21 ka (Fig. 7; input data: Appendix E), both as a test of a different climate and geography and as an initial condition for transient simulations demonstrated in Section 6.3.

From 30 to 20 ka, sea level and ice extent changed relatively little compared to the deglaciation that followed (Lambeck

360 et al., 2014). Therefore, although it is still unlikely that the water table was fully at a steady-state, it is a more reasonable assumption at the LGM than in any subsequent time until the Late Holocene. To reach steady-state, we ran this simulation for over 20,000 years, again noting that this is significantly longer than the present-day global median groundwater response time of 5727 years (Cuthbert et al., 2019a). As before, we evaluated the e-folding response time within our LGM simulation of North America, and found it to be 4559 years.
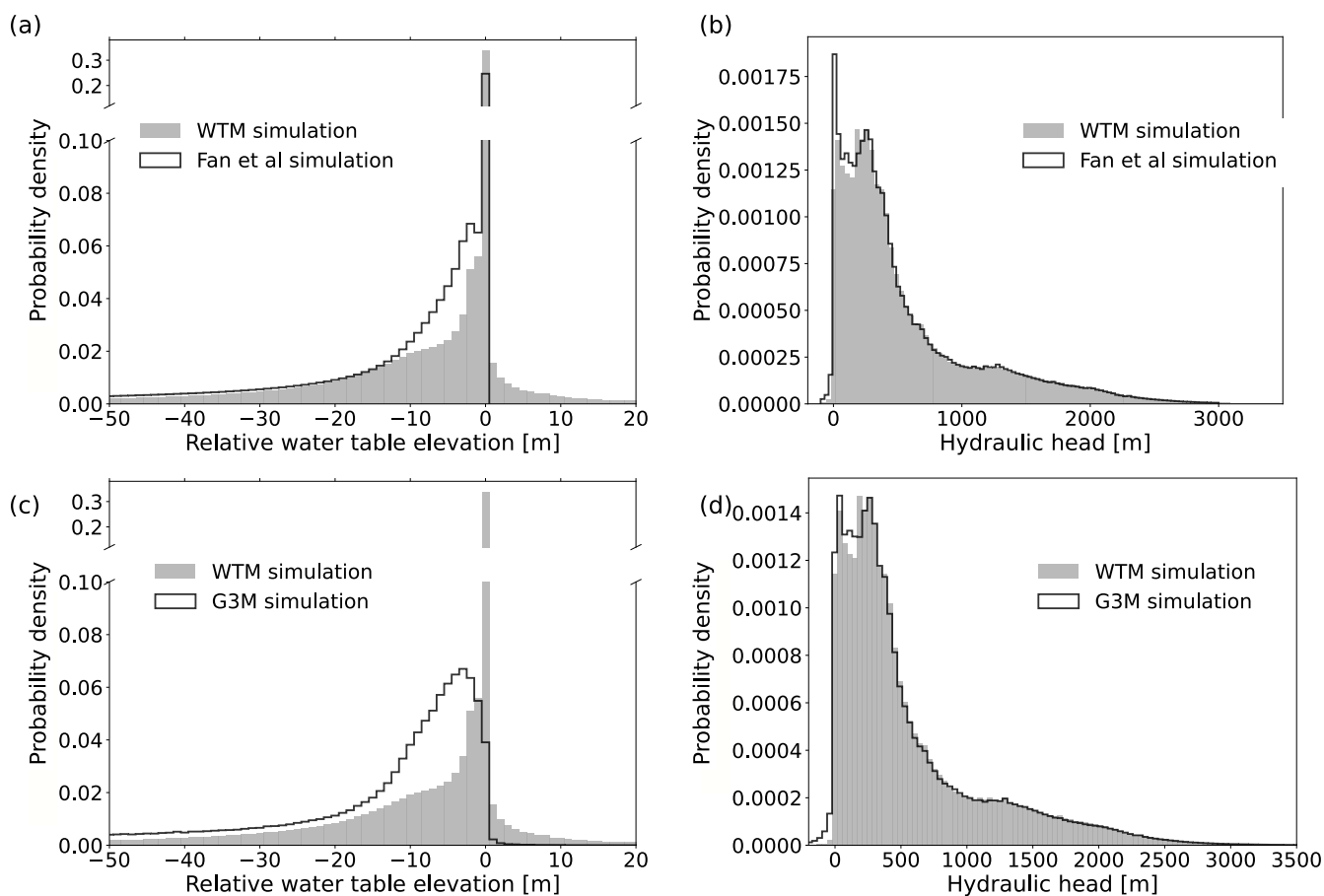
Figure 6. Comparing the WTM-computed present-day results against (a,b) the Fan et al. (2013) simulation results and (c,d) G3M simulation results. These histograms compare probability density functions of relative water-table elevation (left column) and hydraulic head values (right column), with the WTM simulations in shaded grey and the other simulations as a black line. Note the y-axis break in (a) and (c) to accommodate the peak of near-0 values.
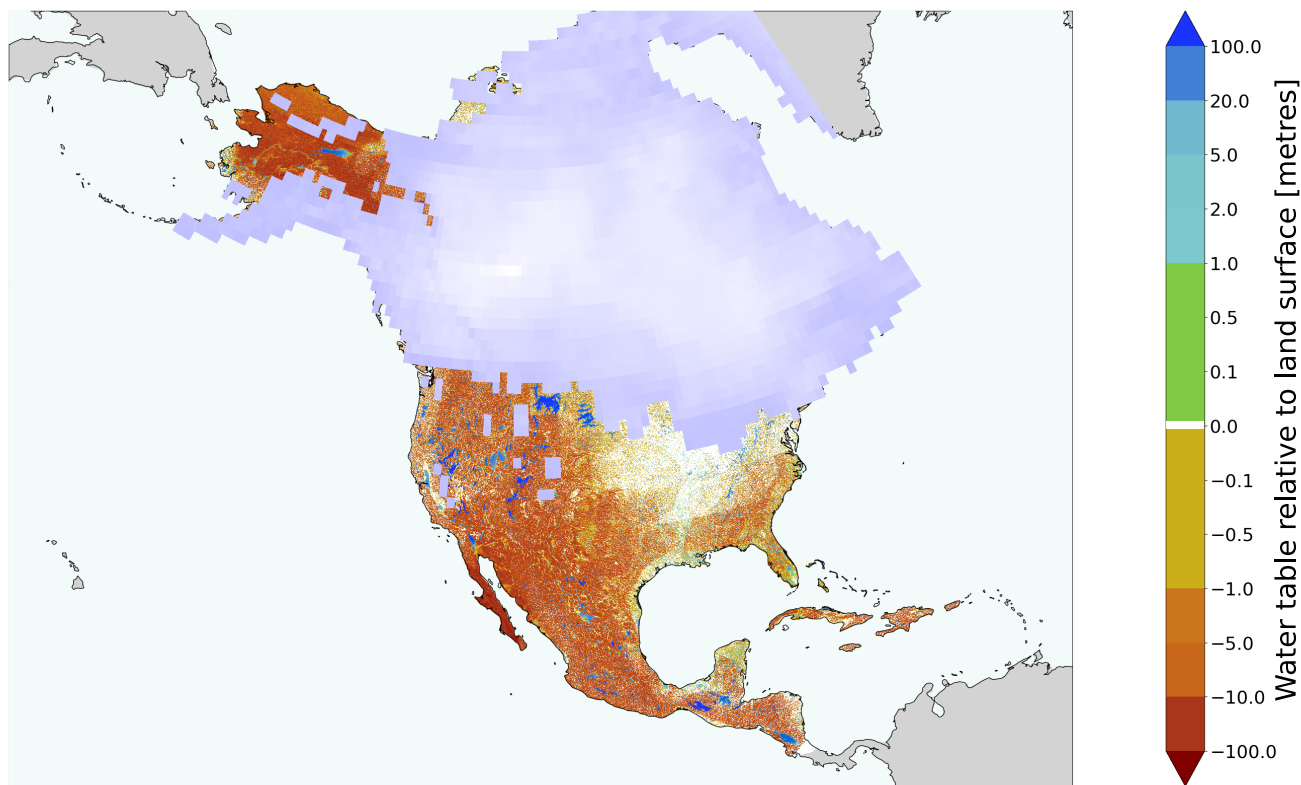
Figure 7. Simulated water table for North America at the LGM (21 ka). Positive values indicate lake depths and negative values indicate the depth of groundwater tables beneath the land surface. The basemap includes ocean (pale cyan) and land (grey). Continental ice thickness from ICE-6G (Peltier et al., 2015) varies from blue-grey (thin) to white (thick).

365   In the same way as the present day simulation, we computed the groundwater table using 0.1-year time steps and updated surface water using FSM once per year. The spatial resolution used was 30 arcseconds. Results of this simulation are shown in Fig. 7.

    In comparison with the present-day climate-driven water table shown in Fig. 3, the LGM water table is noticeably higher in the eastern portions of the continent, and there is significantly more lake-water visible in the west and south (Fig. 8(a)). Note

370   also the larger ice extent and lower sea level at LGM. Broadly speaking, the changes in water table depth matches changes in $P - ET$ (precipitation minus evapotranspiration) (Fig. 8(b)). Most regions with increased $P - ET$ experienced rising water tables, and vice versa. The ice sheets and associated glacial isostatic adjustment also played a role: Ice thickness provided a pressure head that drove both surface-water and groundwater flow, and its melt both added water and altered the "topography", which here also includes ice-sheet contributions to driving flow (see LGM ice extent on Fig. 7 and Fig. 8). GIA primarily

375   caused land uplift in the simulated time period, thereby increasing elevation head. The higher head values in northern North

America at LGM (from overlying ice) may have played a role in moving groundwater further south – consistent with the model-based findings of Lemieux et al. (2008) – resulting in higher water tables to the south of the ice sheet margin at that time.

380   In total, water tables at the LGM are higher than those in the present day (Fig. 3), with the difference between the two simulations amounting to 6.0 cm SLE (approximately 21.8 million billion litres of water). Over this time period, lake storage increased by 5.8 cm SLE – predominantly as a result of the Great Lakes becoming deglaciated. Despite this change in lake volume, we can observe in Fig. 7 that many now-vanished lakes existed, especially along the ice margin and in now-arid regions. Meanwhile, groundwater storage decreased by 11.8 cm SLE from the LGM to the present day. This change appears to be largely driven by changes in climate. Note that both simulations assumed a steady-state water table and this result may be

385 different when simulating a transient change in water table.

6.3   Transient run: Changes in the North American water table over 5,000 years

We demonstrate the transient-simulation mode of the WTM by evolving the North American water table for 5,000 years, starting from its 21 ka steady state (see Fig. 9). During this early portion of the deglaciation (21 ka to 16 ka), warming climate (He, 2011) led to modest ice-sheet retreat (Peltier et al., 2015). Sea level slowly began to rise (Austermann et al.,

390 2013; Gorbarenko et al., 2022). The initialisation of ice-sheet retreat and associated glacial isostatic adjustment permitted significant growth of proglacial lakes (Austermann et al., 2022). Changing climate and ice volume would also naturally impact groundwater storage.

    In our simulation, water-table elevation generally decreases, especially at the southern tip of the continent, closely matching the changes in $P - ET$. Mean water table for the continent dropped by 0.8 metres from -2.73 m to -3.53 m. Total ground-

395 water and lake-water storage in North America decreased by 4.3 cm SLE (see Fig. 10). This decrease was predominantly in groundwater (4.5 cm SLE), while lake storage saw a slight increase (0.2 cm SLE). Lake migration is visible – Fig. 9 shows a small area of increased water table just to the north of a small oval of decreased water table as a lake shifts with the melting ice sheet. The most rapid change in groundwater storage occurred from 17 to 16.5 ka, following 500–1000 years after a rapid drop in $P - ET$ in the inputs from the TraCE-21K climate simulation (He, 2011) associated with Heinrich Event 1. In these sim-

400 ulated inputs, the meltwater-forced reduction in Atlantic Meridional Overturning Circulation (AMOC) strength corresponded to a continentally averaged ∼15% reduction in precipitation relative to the Last Glacial Maximum (see Fig. 10).

7   Conclusions

Long-term change in the water table impacts the whole hydrologic cycle, including sea level and climate. Despite this, little is known about the changing water table over time scales longer than decades. The WTM provides the new capability to compute

405 long-term, continental-scale changing water tables and terrestrial water storage. The WTM's simple input requirements mean that it can simulate water tables in the distant past or in the future as climate continues to change. Initial model runs indicate
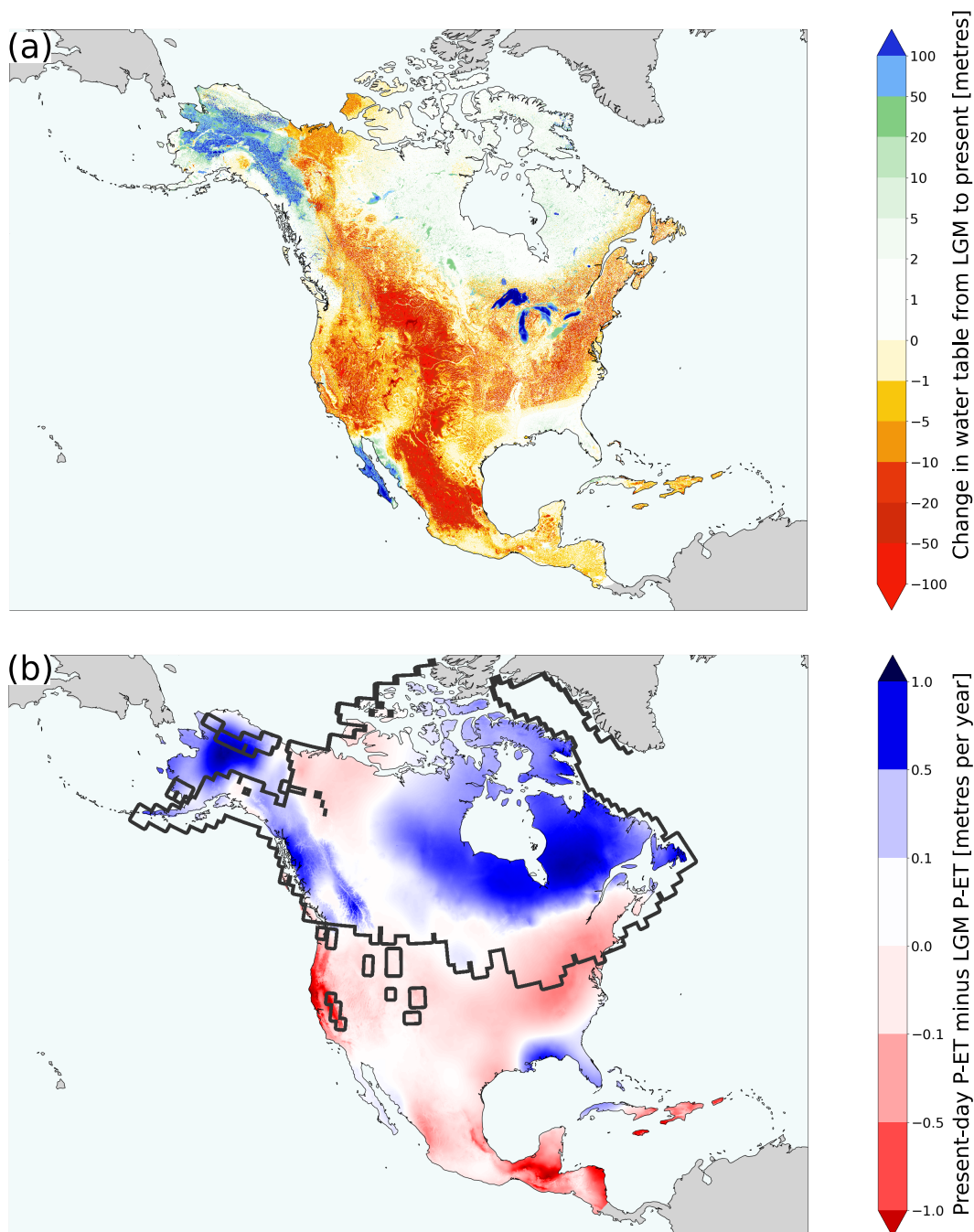
Figure 8. Present day climate-driven water table minus LGM water table (a). The Great Lakes filled with water following their deglaciation. Warmer and drier climate (b) reduces terrestrial water storage more broadly, and especially in the west. The solid dark grey line on panel (b) represents the ice extent at LGM.
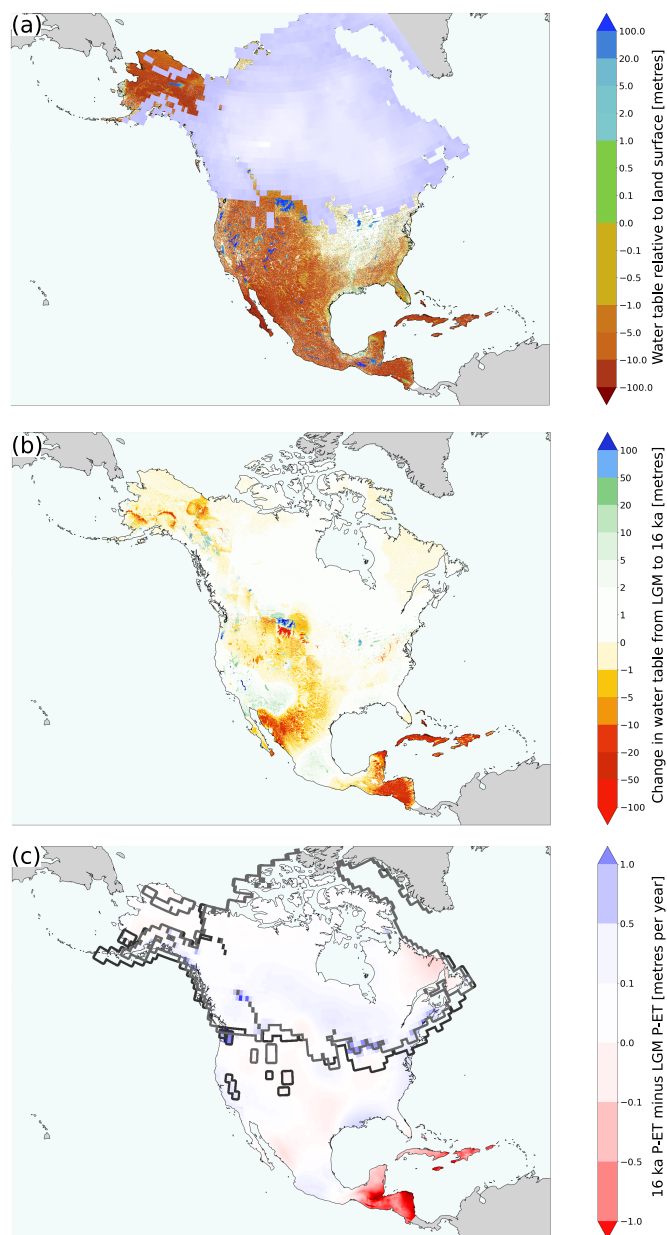
Figure 9. Water table depth at 16 ka, and change since the LGM. (a) shows simulated water table for North America at 16 ka. Positive values indicate lake depths and negative values indicate the depth of groundwater tables beneath the land surface. The basemap includes ocean (pale cyan) and land (grey). Continental ice thickness from ICE-6G (Peltier et al., 2015) varies from blue-grey (thin) to white (thick). In (b), the change in water table since the LGM is visualised (16 ka water table minus 21 ka water table). (c) shows the change in P-ET from 21 ka to 16 ka. The 21 ka ice margin is shown in dark grey, and the 16 ka ice margin, which sometimes lies atop the 21 ka ice margin, is shown in medium grey.
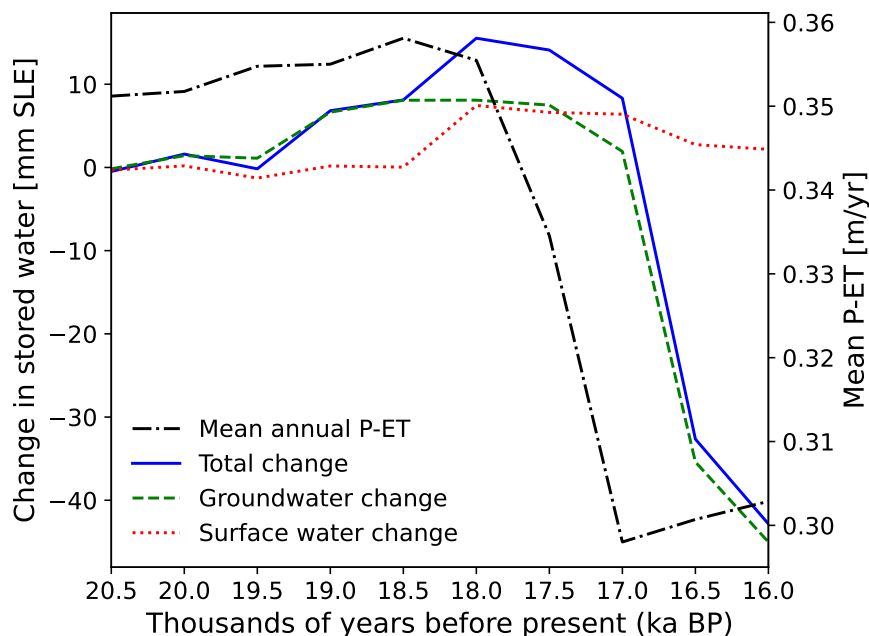
Figure 10. Changes in stored water as a sea level equivalent and mean annual P-ET throughout the transient simulation. The total change in stored water is the sum of the groundwater and surface-water changes. P-ET is scaled to the secondary y-axis.

that water storage across a continent can change by several centimeters SLE under natural climate change, and that changes in water-table depth broadly follow the patterns of changing $P - ET$.

Code availability. Complete, well-commented source code for the WTM is available on GitHub (https://github.com/KCallaghan/WTM/,
410   v2.0.1) and Zenodo (https://doi.org/10.5281/zenodo.10611076, v2.0.1).

Appendix A: Model inputs, logical flow, and outputs

A1   Data input requirements

The WTM requires the following 2D, horizontally distributed input arrays for all steady-state or transient model runs:

- **Topography:** Land elevation above sea level [metres]. At the user's discretion, this may be modified to include overlying
415   ice.

- **Slope:** Topographic slope, which should be based on the input topography data [unitless].

- **Ocean mask:** A binary mask with 1 values indicating land cells and 0 values indicating ocean cells.

- **Climatic water input:** Precipitation and, if appropriate, ice melt or any other water entering the system [metres per year].

420 - **Evapotranspiration:** Evapotranspiration occurring over land (actual ET) [metres per year].

- **Open-water evaporation:** The evaporation that will occur when there is open surface water (i.e. a lake: Appendix D) (potential ET) [metres per year].

- **Winter temperature:** Temperature during the months of December, January, and February (Northern hemisphere) or June, July, and August (Southern hemisphere) [°C].

425 - **Shallow sub-surface hydraulic conductivity – horizontal:** Horizontal hydraulic conductivity ($K_{1.5}$ in Equation 5), representative of near-surface conditions [metres per second].

- **Porosity:** Shallow sub-surface porosity (ϕ in Equation 9) [unitless].

For transient model runs, separate input arrays are required for the start and end times for topography, slope, climatic water input, evapotranspiration, open-water evaporation, winter temperature, and runoff ratio (optional). The values of these arrays 430 will change linearly through time from the start to the end values. In addition, transient model runs require a starting relative water-table elevation.

In some cases, the following optional input data may be used:

- **Starting relative water-table elevation:** This input, required for transient model runs, is also provided as an option for steady-state runs. This allows users to reach steady-state more rapidly if there is some initial knowledge about the 435 water table; or it allows users to break the model run up into several shorter runs by using previous outputs as an input for this array. The relative water-table elevation (z_{wr}) is defined as the water-table elevation minus the elevation of the land surface [metres]. Positive values indicate the presence of a lake, while negative values indicate groundwater table. If this input is not supplied, z_{wr} will be initialised at 0 (equal to the land surface) and the model should first be run to steady-state before any transient model runs can be performed.

440 - **Runoff ratio:** (optional, at user's discretion). If provided, precipitation minus evapotranspiration (P-ET) will be split into groundwater recharge and overland runoff using this array of runoff ratios. If not provided, all P-ET is used as recharge and is added directly to the groundwater table in the cell in which it falls.

- **Shallow sub-surface hydraulic conductivity – vertical:** (optional: only required if the infiltration option is enabled, Section 4.2.1) Vertical hydraulic conductivity, representative of near-surface conditions [metres per second]. If this input 445 is not provided, the infiltration option must be disabled.
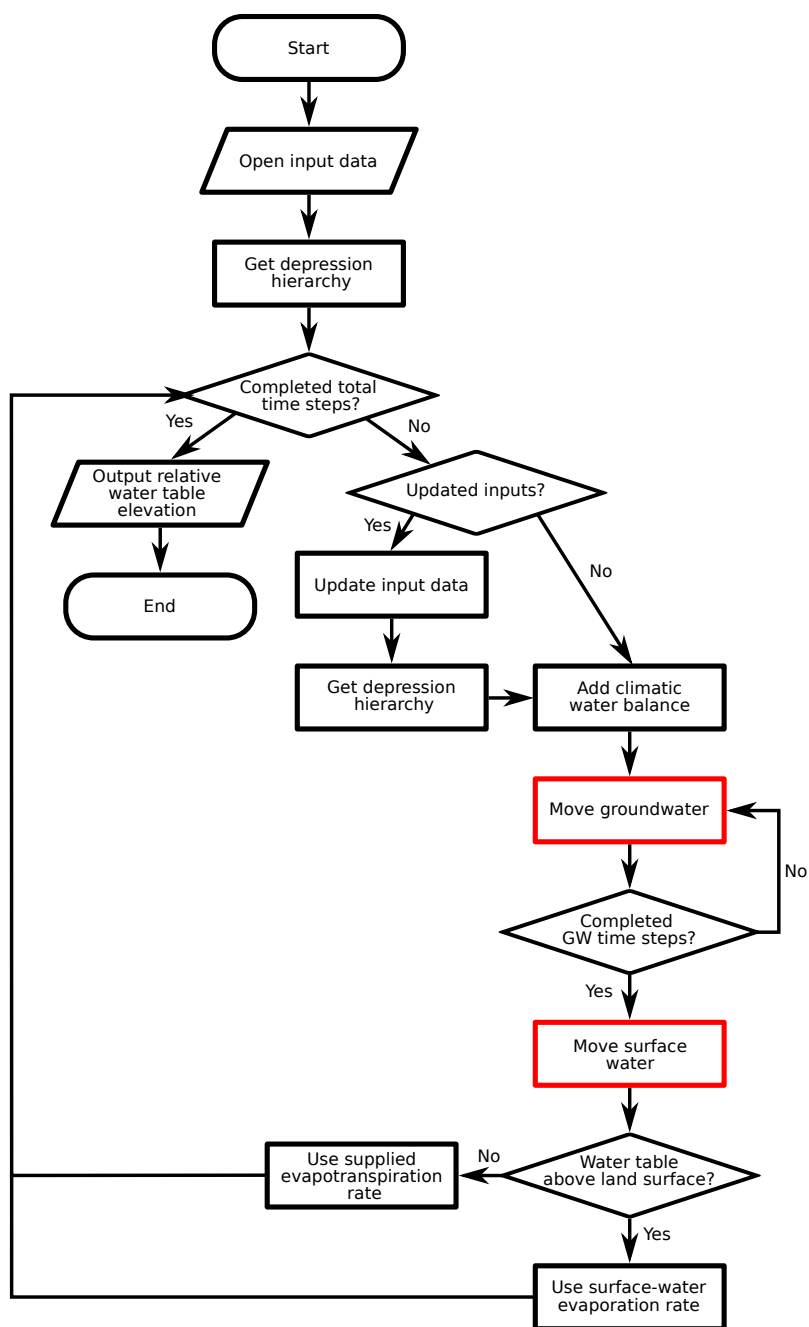
Figure A1. Steps taken by the WTM. The two red boxes indicate the components used to couple groundwater and surface water.

A2 Logical flow

The logical flow of the WTM is shown in Fig. A1. Model inputs, as described in Appendix A1, are provided and the depression hierarchy for the given topography is calculated. In transient runs, the input files are updated through time as conditions change; the depression hierarchy is recalculated as topography changes. The model then adds the appropriate recharge to

450   the water table and moves groundwater, moves surface water, and then calculates the climatic water balance (precipitation minus evapotranspiration, plus icemelt or any other water inputs/outputs) for the next time step. The evapotranspiration field is updated to use the Penman-equation result (Appendix D) ('open water evaporation' input file) wherever the the water table lies above the surface, and the evapotranspiration input file elsewhere. The model concludes after it reaches the prescribed total number of time steps. At this point, it writes outputs to file. Outputs are also saved at regular intervals throughout the model

455   run.

A3 Outputs

The WTM generates two outputs:

- Relative water-table elevation (gridded raster), saved at the end of the model run and at regular intervals throughout.

- A text file recording the number of cycles completed and the amount of water table change occurring during each step

460   of the simulation.

Appendix B: Solving the non-linear groundwater equation

We solve for the change in groundwater head through time using the 2D horizontal groundwater equation for saturated groundwater flow in an unconfined aquifer, in a heterogeneous medium, which is assumed to be horizontally isotropic due to a lack of directional data for hydraulic conductivity (Freeze and Cherry, 1979). We invoke the Dupuit-Forchheimer theory of free-

465   surface flow, which works on two assumptions: (1) flow is horizontal, and (2) the hydraulic gradient is equal to the gradient of the water table surface and does not vary with depth. The equation is:

$$S_y \frac{\partial h}{\partial t} = \frac{\partial}{\partial x}\left(T\frac{\partial h}{\partial x}\right) + \frac{\partial}{\partial y}\left(T\frac{\partial h}{\partial y}\right) + R, \tag{B1}$$

where h is the groundwater head, T is the transmissivity, t is the length of a single time interval, x and y are the two dimensions of groundwater movement, R is recharge, and S_y is the specific yield of the aquifer, here approximated as being

470   equal to porosity. Note that our assumptions that the aquifer is unconfined and that groundwater flows in two dimensions allows us to use T in this formula, where $T = Kh$ and K is the hydraulic conductivity. More information about our treatment of Transmissivity is given in Section 3.2.

When using the Dupuit-Forchheimer approximation, discharge, Q, is defined as:

$$Q = -T\frac{\Delta h}{\Delta d} \tag{B2}$$

475 (Freeze and Cherry, 1979, Equation 5.28), where Δd refers to the distance in either the x (S–N) or y (W–E) direction, as appropriate.

Combining equations B2 and B1 gives:

$$S_y \frac{\partial h}{\partial t} = -\frac{\partial Q_x}{\partial x} - \frac{\partial Q_y}{\partial y} + R. \tag{B3}$$

Defining Q for each of the cardinal directions gives:

480
$$Q_E = -T_{i+1/2} \left(\frac{h_{t(i+1,j)} - h_{t(i,j)}}{\Delta x} \right) \tag{B4}$$

$$Q_W = -T_{i-1/2} \left(\frac{h_{t(i,j)} - h_{t(i-1,j)}}{\Delta x} \right) \tag{B5}$$

$$Q_N = -T_{j+1/2} \left(\frac{h_{t(i,j+1)} - h_{t(i,j)}}{\Delta y} \right) \tag{B6}$$

$$Q_S = -T_{j-1/2} \left(\frac{h_{t(i,j)} - h_{t(i,j-1)}}{\Delta y} \right) \tag{B7}$$

Here, i is the cell index along the x (S–N) axis and j is the cell index along the y (W–E) axis. Note that we assess T at cell
485 boundaries rather than at the cell centres. We do this because mass transfer occurs across these cell boundaries, so calculating the gradients here provides more accurate directional water discharges. We indicate this cell-boundary-based calculation with the $+/-1/2$ subscripts.

Substituting these definitions of Q into Equation B3 and expanding the left-hand side gives:

$$S_y \frac{h_{t+1(i,j)} - h_{t(i,j)}}{\Delta t} = T_{(i+1/2)} \left(\frac{h_{t(i+1,j)} - h_{t(i,j)}}{\Delta x^2} \right) - T_{(i-1/2)} \left(\frac{h_{t(i,j)} - h_{t(i-1,j)}}{\Delta x^2} \right) +$$
490
$$T_{(j+1/2)} \left(\frac{h_{t(i,j+1)} - h_{t(i,j)}}{\Delta y^2} \right) - T_{(j-1/2)} \left(\frac{h_{t(i,j)} - h_{t(i,j-1)}}{\Delta y^2} \right) + R. \tag{B8}$$

Solving for head at the next time step, h_{t+1}, gives:

$$h_{t+1(i,j)} = \left[T_{(i+1/2)} \left(\frac{h_{t(i+1,j)} - h_{t(i,j)}}{\Delta x^2} \right) - T_{(i-1/2)} \left(\frac{h_{t(i,j)} - h_{t(i-1,j)}}{\Delta x^2} \right) + \right.$$
$$\left. T_{(j+1/2)} \left(\frac{h_{t(i,j+1)} - h_{t(i,j)}}{\Delta y^2} \right) - T_{(j-1/2)} \left(\frac{h_{t(i,j)} - h_{t(i,j-1)}}{\Delta y^2} \right) + R \right] \frac{\Delta t}{S_y} + h_{t(i,j)}. \tag{B9}$$

This equation is now broken down into the thing that we want (h_{t+1}), and things that we know. We solve the equation using
495 the PETSc SNES solver (Balay et al., 1997, 2022a, b).

Appendix C: Infiltration of surface water

C1 Transit time across a cell

To calculate the amount of infiltration that happens while water is in transit across a cell, we must consider the total time the water takes to cross the cell. The more time that the water spends in a cell, the longer it will have to infiltrate. Water will take

longer to flow across cells that are larger or have shallower slopes, or when the water depth, and hence its flow velocity, is smaller.

We use Manning's equation to estimate the time taken for flow to cross a cell.

$$u = \frac{1}{n} R_h^{2/3} S^{1/2}, \tag{C1}$$

where u is the mean (i.e. vertically averaged) velocity of the surface water moving across the cell, n is the Gauckler–Manning coefficient, R_h is the hydraulic radius, and S is the slope. By default, we set Manning's n to a value of $0.05\,m^{-1/3}s$. We make the assumption that the height of water in the cell, h, is much smaller than the cell width. This allows us to simplify the hydraulic radius to equal h:

$$u = \frac{1}{n} h^{2/3} S^{1/2}. \tag{C2}$$

Because S and n are both constants, for convenience we will combine them in constant k_0, where

$$k_0 = \frac{S^{1/2}}{n}, \tag{C3}$$

so that

$$u = k_0 h^{2/3}. \tag{C4}$$

The next step is to consider the infiltration rate,

$$\frac{\mathrm{d}h}{\mathrm{d}t_I} = -k_{\mathrm{sat}}. \tag{C5}$$

By separating variables, integrating, and defining $h = h_0$ at $t_I = 0$, we obtain:

$$h = h_0 - k_{\mathrm{sat}} t_I. \tag{C6}$$

We substitute Eq. C6 into Eq. C4 and use the definition of velocity as the time derivative of position to set up the final equation to integrate:

$$\frac{\mathrm{d}L}{\mathrm{d}t} = k_0 \left(h_0 - k_{\mathrm{sat}} t_I \right)^{2/3}. \tag{C7}$$

where L is the displacement in an arbitrary orientation. By separating variables and solving via u substitution, we obtain:

$$
\begin{aligned}
L &= k_0 \int_0^{t_i} (h_0 - k_{\mathrm{sat}} t_I)^{2/3} dt \\
&= -\frac{3}{5} \frac{k_0}{k_{\mathrm{sat}}} (h_0 - k_{\mathrm{sat}} t_I)^{5/3} + c,
\end{aligned}
\tag{C8}
$$

where c is the constant of integration. Defining $L = 0$ when $t_I = 0$ (i.e. that the clock starts when the water first touches the cell margin), we obtain:

$$c = \frac{3}{5} \frac{k_0}{k_{\mathrm{sat}}} h_0^{5/3} \tag{C9}$$

525 This gives the distance crossed by the water as:

$$L = \frac{3}{5}\frac{k_0}{k_{\text{sat}}}\left(h_0^{5/3} - (h_0 - k_{\text{sat}}t_I)^{5/3}\right). \tag{C10}$$

We rearrange this expression to find the amount of time that this transit takes, because this is the amount of time that the water has to infiltrate within the cell. Solving for the transit time and substituting S and n back in gives

$$t_I = \left[h_0 - \left(h_0^{5/3} - \frac{5}{3}\frac{n}{S^{1/2}}k_{\text{sat}}\Delta L\right)^{3/5}\right]\bigg/ k_{\text{sat}}. \tag{C11}$$

530 In the WTM, we limit the topographic slope, S, to a minimum value of 10^{-6} to allow movement over flat cells in the DEM. We calculate L based on the directions of travel between the two cells (north–south, east–west, or diagonal), and the latitude of the cells.

C2 Infiltration

We now know the time t_I that it takes the water to cross a cell as a function of the distance travelled by the water from cell 535 to cell (L), slope (S), and flow depth (h). When water flows across a cell that is not already groundwater-saturated, the flow depth will decrease as it crosses the cell due to infiltration. This occurs at a rate governed by the saturated vertical hydraulic conductivity (k_{sat}); for simplicity, we do not consider transient wetting and drying effects in the unsaturated zone. Some water will infiltrate and some will continue to flow downslope as infiltration-excess overland flow (Horton and Htrata, 1955). When water crosses a cell that is already fully saturated, i.e. the groundwater table is at the land surface, no infiltration is possible and 540 saturation-excess overland flow (Dunne and Black, 1970) will occur.

There are two possible solutions for the potential total amount of water infiltrated, I_{pot}:

$$I_{\text{pot}} = \begin{cases} h_0 & \text{if } h_0^{5/3} \le \frac{5}{3}\frac{n}{S^{1/2}}k_{\text{sat}}\Delta L \\ k_{\text{sat}}t_I & \text{otherwise.} \end{cases} \tag{C12}$$

In the first case, the entire column of water that enters the cell can infiltrate before it crosses. For the '=' sub-case, the travel time is precisely the infiltration time; for the '<' sub-case, the solution to Equation C11 becomes undefined because the water 545 all infiltrates before completing its crossing. In the second case, the potential infiltration simply equals the saturated hydraulic conductivity multiplied by the amount of time that this water can infiltrate before it crosses the cell; remaining water continues to flow into the next cell.

Converting I_{pot} to the actual amount of infiltration that occurs, I, requires consideration of the space available to accommodate infiltration water. Combining Eq. C12 with the amount of groundwater space available in the cell, given by $-\phi z_{wr}$ where 550 ϕ is the subsurface porosity (assumed constant with depth) and z_{wr} is the relative water table elevation, provides the general solution:

$$I = \min\left(-\phi z_{wr}, I_{\text{pot}}\right). \tag{C13}$$

This amount of infiltrated water is then subtracted from the flow depth, h. If $h > 0$ as the water exits the cell, then it continues onwards to the next downslope cell.

Appendix D: Open-water evaporation

We calculate open-water evaporation by solving and applying the Penman Equation (Dingman, 1994) alongside the Charnock (1955) expression for the roughness length over open water as a function of wind-induced waves. This evaporation rate overrides the input evapotranspiration rate wherever the water table crops out above the ground surface, forming an exposed water body (Fig. A1). The effects of ice cover are not considered.

The Penman (1948) Equation combines radiative, sensible, and latent heat transfer to solve for evaporation. Though it is well-established (Finch and Calver, 2008; Valiantzas, 2006; Vörösmarty et al., 1998; Zotarelli and Dukes, 2010), we choose to include a brief derivation of the Penman equation due to (1) the central role played by evaporation in our study; (2) the fact that most derivations center on the Penman–Monteith equation (Monteith, 1965), which involves plant transpiration that is not relevant to our application to lakes; and (3) our inclusion of a wind-speed-determined roughness length to modulate wind-driven turbulent energy transfers, which seems reasonable to include but that we have not found in our review of the literature. Here we use variable nomenclature that is more common to thermodynamics than to hydrology.

D1 Penman Equation (general form)

The Penman Equation relates evaporation rate (E), which is a latent-heat flux, to net-radiation flux (R_n: incoming and outgoing shortwave and longwave) and sensible heat flux due to turbulent atmospheric heat transfer ($Q_{H,s}$, where subscript H indicates enthalpy and s indicates that it is sensible):

$$E = \frac{R_n - Q_{H,s}}{\rho_w \Delta H_{\text{vap}}}. \tag{D1}$$

Here, ρ_w is water density, and ΔH_{vap} is latent heat of vaporization of water. These terms in the denominator act to convert the energy fluxes [W m^{-2}] into evaporation [m s^{-1}].

D2 Input data products

Inputs for our solution come from the TerraClimate and GEBCO_2020 datasets. TerraClimate (Abatzoglou et al., 2018) comprises monthly 2.5-arcminute (∼5 km N–S) gridded data products for:

- Incoming solar (shortwave) radiation

- Monthly averaged minimum and maximum daily temperatures

- Wind speed

- Vapor pressure

GEBCO_2020 (GEBCO Bathymetric Compilation Group, 2020) is a 15-arcsecond (∼0.5 km N–S) global gridded topographic and bathymetric dataset. We resampled this to 2.5 arcminutes to match the resolution of TerraClimate.

D3 Net radiation

In the field, acquiring net radiation requires paired upward- and downward-facing pyranometers and pyrgeometers to measure
incoming and outgoing shortwave and longwave radiation. Here we use a combination of calculations and remotely sensed data
products to assemble a solar-radiation data product at an appropriate resolution for our contiental-scale modeling example.

TerraClimate (Abatzoglou et al., 2018) provides the incoming shortwave radiation flux, $R_{in,s}$. Outgoing shortwave radiation
equals the incoming radiation times the surface albedo α. Therefore, net shortwave radiation, $R_{n,s}$, is given by

$$R_{n,s} = (1 - \alpha) R_{in,s}. \tag{D2}$$

We use $\alpha = 0.06$ as characteristic of open water.

We lack data on net longwave radiation, $R_{n,l}$, but know that (1) outgoing longwave flux is proportional to surface temperature
via the Stefan–Boltzmann Law and (2) that incoming longwave radiation is related to greenhouse gases in the atmosphere that
absorb and re-emit this outgoing radiation. We therefore follow and modify the approach taken by Zotarelli and Dukes (2010)
in approximating the surface temperature by the maximum and minimum air-temperature values, and using vapor pressure and
cloudiness to estimate the impact of greenhouse gases on longwave absorption and re-radiation:

$$R_{n,l} = \sigma \frac{T_{\max}^4 + T_{\min}^4}{2} \left(0.34 - 0.00014 e_a^{1/2} \right) \mathcal{C}. \tag{D3}$$

Here, σ is the Stefan–Boltzmann constant, T is temperature in Kelvin, e_a is the near-surface atmospheric vapor pressure, and
$\mathcal{C}$ is what we choose to call the "cloud function".

We can estimate the value of the cloud function by the difference between the clear-sky solar radiation, $R_{in,s,CS}$, and the solar
radiation received at the land surface, $R_{in,s}$. To compute the clear-sky solar radiation, we first compute the top-of-atmosphere
(i.e., extraterrestrial) solar radiation ($R_{in,s,TOA}$): see `sunpos.py` from Wickert (2020). We then modify it based on elevation
(Zotarelli and Dukes, 2010), which determines the atmospheric thickness above a particular location:

$$R_{in,s,CS} = \left(0.75 + 2 \cdot 10^{-5} z \right) R_{in,s,TOA}, \tag{D4}$$

where z, as in the main text, is surface elevation in meters.

This method works only where sufficient incoming solar radiation exists to produce a meaningful difference between
$R_{in,s,TOA}$ and $R_{in,s}$. Based on our tests, a reasonable cutoff incoming value of solar radiation is $15\,\mathrm{W\,m^{-2}}$.

$$\mathcal{C} = \begin{cases} 1.35 \frac{R_{in,s}}{R_{in,s,TOA}} - 0.35 & \text{if } R_{in,s,TOA} \geq 15 \\[2ex] \left[1.35 \frac{R_{in,s}}{R_{in,s,TOA}} - 0.35 \right]_{15\text{--}20}, & \text{otherwise} \end{cases} \tag{D5}$$

where the lower term equals the average of the upper term where $15 < R_{in,s,TOA} < 20$. This is an obvious kludge for the sake
of generating a proof-of-concept model outputs, and generates a reasonable but inaccurate cloud-function value for the polar
regions.

The final step is straightforward. Net radiation flux is simply the sum of the net shortwave and longwave fluxes:

$$R_n = R_{n,s} + R_{n,l}. \tag{D6}$$

D4 Sensible heat flux

Deriving the Penman equation for sensible heat flux, $Q_{H,s}$, results in (Dingman, 1994):

$$Q_{H,s} = \frac{K_H u}{\Delta_{P,T}} \left[\frac{E}{K_E u} - (e_{\text{sat}} - e_a) \right]. \tag{D7}$$

Here, K_H and K_E are coefficients of turbulent conductance [$\text{kg m s}^{-1}\,\text{K}^{-1}$] for sensible heat and water vapor (i.e., latent heat), respectively. u is wind speed, which is conventionally measured two meters above the surface. $\Delta_{P,T}$ is the slope of the water liquid-to-vapor phase transition at the air temperature, T_a, which likewise is measured two meters above the surface. Similarly, e_{sat} is the saturation water vapor pressure at T_a, whereas e_a is the actual water vapor pressure.

These turbulent conductance coefficients, K_H and K_E, are defined based on ratios of heat (K_H) and water vapor (K_E) transfer to momentum transfer (Dingman, 1994):

$$K_H = \frac{D_H}{D_M} c_p \rho_a \left(\frac{u_*}{u} \right)^2; \tag{D8}$$

$$K_E = \frac{D_{\text{WV}}}{D_M} \frac{\Delta \rho_a}{P \rho_w} \frac{R_a}{R_v} \left(\frac{u_*}{u} \right)^2. \tag{D9}$$

Here, D_H is thermal diffusivity in air, D_M is diffusivity of momentum, and D_{WV} is diffusivity of water vapor. For a stable atmosphere, which we assume, the same turbulent eddies result in the transfer of heat, momentum, and water vapor. Therefore, $D_H/D_M = D_{WV}/D_M = 1$. This simplifies Equations D8 and D9 to:

$$K_H = c_p \rho_a \left(\frac{u_*}{u} \right)^2; \tag{D10}$$

$$K_E = \frac{\rho_a}{P \rho_w} \frac{R_a}{R_v} \left(\frac{u_*}{u} \right)^2. \tag{D11}$$

To restate the variable definitions from the main text for convenience: c_p is the specific heat capacity of air at constant pressure, ρ_a is air density; u_* is wind shear velocity, u is measured wind velocity (typically at 2 meters elevation above the surface), ρ_w is water density, P is atmospheric pressure, and $R_a/R_v = 0.622$ is the ratio of the gas constants of air and water vapor.

D5 Full Penman Equation

Combining Equations D1 and D7 and solving for evaporation results in the common full form of the Penman Equation (cf. Dingman, 1994):

$$E = \left[R_n + \left(\frac{K_H u}{\Delta_{P,T}} \right) (e_{\text{sat}} - e_a) \right] \Big/ \left[\rho_w \Delta H_{\text{vap}} + \left(\frac{K_H}{K_E} \frac{1}{\Delta_{P,T}} \right) \right]. \tag{D12}$$

Substituting in the definitions of coefficients K_H and K_E, we obtain Equation E1.

D6 Variable water-surface roughness

640 The u_* term in the diffusivity of momentum, D_M, may be evaluated by solving for the boundary-layer velocity profile given by the logarithmic Law of the Wall, in which

$$u(z) = \frac{u_*}{\kappa} \ln\left(\frac{z_\alpha}{z_0}\right). \tag{D13}$$

Here, $\kappa = 0.407$ is von Kármán's constant, z_α is the height of the air about the land surface, and z_0 is a surface roughness length. It is then possible to solve for u_* by knowing the wind velocity – u at a known elevation, $z_\alpha = z_1$, which is typically 2

645 m above the surface – and the surface roughness length scale.

When wind flows over open water, it generates waves, thereby making this roughness length itself a function of wind speed. This makes Eq. D13 nonlinear, thereby adding a complexity not included in models of evaporation over land.

To address this problem, we first turn to Charnock (1955), who found a quadratic relationship between wave-generated z_0 and u_*. Hersbach (2011) expanded this work and defined z_0 over a broader range of conditions by showing that it depends on

650 kinematic viscosity, ν, in light winds and on a shear-velocity-squared (Charnock, 1955) relationship for strong winds:

$$z_0 = K_\nu \frac{\nu}{u_*} + K_{\text{wave}} \frac{u_*^2}{g}, \tag{D14}$$

where the coefficients $K_\nu = 0.11$ and $K_{\text{wave}} \approx 0.018$. We then substitute this expression for z_0 into Eq. D13 and solve for u_* using the known u at elevation z_1:

$$u_* = \kappa u \left/ \ln\left(\frac{z_1}{K_\nu \nu / u_* + K_{\text{wave}} u_*^2 / g}\right)\right.. \tag{D15}$$

655 With our single known wind speed at z_1=2 meters elevation (Abatzoglou et al., 2018), we can solve this equation for u_* in one of two ways. First, we can use a numerical root finder. We implement this using the `root_scalar` method within Scipy (Wickert, 2020; Virtanen et al., 2020) (see https://github.com/umn-earth-surface/TerraClimate-potential-open-water-evaporation). The second option is to derive an analytical solution. This is possible for the original Charnock (1955) relationship using a Lambert W function, but is not possible for the form given by Hersbach (2011). Roots to Equation D15 exist and are numerically

660 attainable for wind velocities less than approximately 55 m s^{-1}.

Appendix E: Model input data

We performed a steady-state WTM simulation for North America in the present day; a steady-state WTM simulation for North America at the LGM; and transient model runs for the 5000-year period from 21 ka to 16 ka. The required input data arrays are listed in Appendix A1. We provided input data for the transient simulations at 500-year intervals. Here, we chronicle the

665 data sources that were used for each of the required input arrays.

E1 Topography

For the present day simulation, we obtained topographic data from the GEBCO 2020 grid (GEBCO Bathymetric Compilation Group, 2020), which we coarsened from 15 arcsecond to 30 arcsecond resolution by averaging each set of four original grid-cell

elevations within each of our 30-arcsecond grid cells. We added lake bathymetry to this DEM using data from the Global Lake Database (Kourzeneva et al., 2012), using all included lakes except for the Great Lakes, whose bathymetry is already included in GEBCO 2020, and the Great Salt Lake. We updated the bathymetry of the Great Salt Lake using data from Tarboton (2017). At locations where ice exists, we consider the topography under the ice and add the impact of the ice on water flow in the form of an added pressure head. To do so, we use the difference between the ETOPO1 (Amante and Eakins, 2009; Center, 2009) ice-free and ice-included topographies to obtain ice thickness. We subtract this ice thickness from the GEBCO2020 topography, and then add back the ice thickness multiplied by the ratio of ice to water density (0.9167/0.9998). This gives the final topography with added ice pressure head.

We computed topographic change resulting from Glacial Isostatic Adjustment (GIA) based on the ICE-6G (Peltier et al., 2015) ice history and a spherically symmetric viscosity structure with an elastic lithospheric thickness of 96km, an upper mantle viscosity of 0.5×10^{21} Pa s and a lower mantle viscosity of 20×10^{21} Pa s. We used the GIA algorithm described in Kendall et al. (2005) and Dalca et al. (2013) with a maximum spherical harmonic degree of 256 to compute relative sea level across the globe at the LGM and each of the time steps used in our WTM simulations. After interpolating these GIA anomalies to 30-arcsecond resolution, we subtracted them from the modern-day topography described above to obtain a past topography at the LGM and every 500 years after the LGM. Following this, we used the ICE-6G ice history for each time step to compute and then add ice pressure head in order to produce the final set of 'topographic' (topography + ice-pressure head) inputs for the WTM.

E2 Slope

We computed the slope input files using the topography described above, modified by GIA if needed, but without ice included, using GRASS GIS (Neteler et al., 2012). We used the ice-free slope becuase within WTM, the slope data input is only used to determine the appropriate e-folding depth (described in Section 3.2) to use in association with hydraulic conductivity. Water flow directions are computed directly from the topography described above.

E3 Ocean mask

The ocean masks were created using the topography data described above. Any cells that were below sea level, and that could also be grouped into a polygon of below-sea-level cells that touched the edges of the map, were classed as 'ocean' cells. This allowed land cells that were below sea level to still be classed as 'land' (cf. Wickert et al., 2013).

E4 Climatic water input

For the present day, we obtained precipitation data from the Terraclimate dataset (Abatzoglou et al., 2018). We summed averaged monthly data from Terraclimate over a total of 30 years, from 1981 to 2010 inclusive, to obtain annual averages. We resampled the spatial resolution of the Terraclimate from 1/24 degrees (150 arcseconds) to 30 arcseconds using a bivariate spline approximation.

700   For the past, we used modelled precipitation data from the TRACE-21-K simulation (He, 2011). For each time step, we averaged data from 50 years before to 49 years after the given time, obtaining 100-year averages of precipitation. We then did an anomaly correction using the present-day precipitation, described above, for each time step. We resampled data to the 30-arcsecond resolution used in these runs using a bivariate spline interpolation.

  For icemelt, we used the ICE-6G ice model (Peltier et al., 2015). At each time step, we assessed icemelt over the preceding
705   500 years, and converted this to an average annual icemelt. We added this value to the annual precipitation to obtain the total climatic water input.

E5   Evapotranspiration

For the modern day, we obtained evapotranspiration data from the Terraclimate dataset (Abatzoglou et al., 2018) and processed it in the same way as described for precipitation above.

710   For the past, we used modelled evapotranspiration from the TRACE-21-K simulation (He, 2011). As with precipitation, above, we obtained 100-year averages and then performed an anomaly correction of the data relative to the present day. We resampled data to our 30-arcsecond resolution using a bivariate spline approximation.

E6   Open-water evaporation

We calculated evaporation of surface water using the classic Penman (1948) equation, modified following Hersbach (2011) to
715   account for variable water-surface roughness due to wind-driven waves:

$$E = \frac{R_n + (c_p \rho_a u_*^2)/(\Delta_{P,T} u)}{\rho_w \Delta H_{\mathrm{vap}} + P c_p \rho_w (R_v/R_a)} (e_{\mathrm{sat}} - e_a). \tag{E1}$$

Here, E is the rate of open-water evaporation, R_n is net solar radiation, c_p is the specific heat capacity of air at constant pressure, ρ_a is air density, u_* is wind shear velocity, $\Delta_{P,T}$ is the gradient in temperature–pressure space of the liquid-to-vapor phase transition for water, u is wind velocity (typically at 2 meters elevation above the surface), ρ_w is water density, ΔH_{vap} is
720   the latent heat of vaporization of water, P is atmospheric pressure, $R_v/R_a = 1/0.622$ is the ratio of the gas constants of water vapor and air, e_{sat} is water vapor pressure at saturation, and e_a is water vapor pressure. Appendix D holds our derivation.

  For the present day, the open-water evaporation calculations were based on data from TerraClimate (Abatzoglou et al., 2018) and the GEBCO Bathymetric Compilation Group (2020) elevation data set. The open-water evaporation rates were calculated from monthly climatic data from 1958 to 1970, inclusive.

725   For the past, the open-water evaporation calculations were based on climate data from the TraCE-21K simulation (He, 2011). We obtained 100-year averages of open-water evaporation, then performed an anomaly correction relative to the present day and resampled the data to the 30-arcsecond resolution using a bivariate spline approximation.

E7   Winter temperature

For the present day, we used the ERA5 reanalysis monthly mean 0.25 degree latitude–longitude grid data for winter temperature
730   (European Centre for Medium-Range Weather Forecasts, 2019). The data are long-term annual averages, based on monthly

averages from 1979 to 2018 inclusive. To obtain winter temperature, we used monthly temperatures from December, January and February for the Northern hemisphere. We assumed that temperatures from the ERA5 data matched the mean topography within a 0.25 °cell and resampled these temperatures to 30-arcsecond resolution using the 30-arcsecond resolution topography and a wet adiabatic lapse rate of 5 °C/km (Peirce et al., 1998) relative to these mean temperatures.

735   For the past, we used modelled temperature outputs from the TraCE-21K simulation (He, 2011). We took 100-year averages for each time step, and resampled these to the desired 30-arcsecond resolution using topography and an adiabatic lapse rate as described above. We also performed an anomaly correction relative to the present day.

E8   Shallow-subsurface hydraulic conductivity: horizontal

Hydraulic conductivity values are based on the hybrid STATSGO/FAO soil-texture database available at https://ral.ucar.edu/
740   solutions/products/wrf-noah-noah-mp-modeling-system (last accessed: 10 November 2020), which gives 12 different soil texture categories. We converted these to hydraulic conductivity values using the representative values suggested by Clapp and Hornberger (1978). The value for silt was not provided by Clapp and Hornberger (1978), so we estimated it based on other nearby values and the range of possible values given by Earle (2015). Similarly, we selected the value for bedrock from the range given by Earle (2015). We took the value for 'organic materials' from the value listed as 'peat' by Fan et al. (2007).

745   Due to a lack of past hydraulic conductivity or soil-texture data, we assume that these values do not change significantly over the time intervals that we are interested in studying here. Therefore, we use the same hydraulic conductivity dataset for all time steps.

E9   Porosity

Porosity values are based on the same STATSGO/FAO soil texture database as described above, also using representative values
750   suggested by Clapp and Hornberger (1978), Earle (2015), and Fan et al. (2007). We likewise assume that porosity does not change significantly over the time intervals that we are studying and use the same porosity dataset for all time steps.

E10   Runoff ratio

We computed potential runoff ratios (C) following the formula provided in Liu and Smedt (2004):

$$C = C_0 + (1 - C_0)\frac{S}{S + S_0}, \tag{E2}$$

755   where C_0 is a potential runoff ratio for a near-zero slope (Liu and Smedt, 2004, see), S is surface slope as a percentage, and S_0 is a slope constant for a given land use and soil type (Liu and Smedt, 2004, see). The soil textures from the STATSGO/FAO soil-texture database, available at https://ral.ucar.edu/solutions/products/wrf-noah-noah-mp-modeling-system, were used in the selection of values for C_0 and S_0. Since land cover is not known by our model, we averaged the values for forest and for grass to obtain a best estimate at all locations. We used the slopes described above for each time step. The values for C_0 and
760   S_0 are considered to be constants over the time period we are studying.

E11   Starting relative water-table elevation

Starting relative water-table elevation data is a requirement for the transient simulations. We used the output of the steady-state simulation at 21 ka as the starting relative water-table elevation for the transient simulation. We saved the water table result at 500-year intervals, using the new result as the input for the next 500-year simulation each time.

765   ### E12   Vertical hydraulic conductivity

We opted not to enable the infiltration option for this set of model runs, therefore no vertical hydraulic conductivity input was needed. It is possible to obtain these from horizontal hydraulic conductivity values using anisotropy values, such as those listed by Fan et al. (2007).

E13 e-folding constants

770   Calibration constants for the e-folding depth were set to $a = 100$, $b = 150$, and $f_{\min} = 2.5$, following Fan et al. (2013).

Author contributions.   AW and KLC conceptualised the WTM. KLC, AW and RB conceptualised FSM, which was co-written by KLC and RB (algorithm design led by RB). Remaining code for the WTM was led by KLC, consulting with all authors. All authors conceptualised the simulation examples shown, and simulations and validation were performed by KLC. AW, JA, and KLC each provided computing resources at various points throughout the project. Writing of the initial draft was led by KLC while all authors reviewed and edited the paper.

775   *Competing interests.*   Some authors are members of the editorial board of GMD.

Acknowledgements.   RB was supported by Lawrence Berkeley National Lab's Grace Hopper Postdoctoral Fellowship in Computing Sciences. Previous work was supported by the Department of Energy's Computational Science Graduate Fellowship (Grant No. DE-FG02-97ER25308) and, through the Berkeley Institute for Data Science's PhD Fellowship, by the Gordon and Betty Moore Foundation (Grant GBMF3834) and by the Alfred P. Sloan Foundation (Grant 2013-10-27). KLC and ADW were supported by the National Science Foundation under grant no.
780   EAR-1903606. ADW received further support through a Humboldt-Forschungsstipendium from the Alexander von Humboldt-Stiftung. KLC and JA were supported by the National Science Foundation under grant no. EAR-1903518. Ying Fan Reinfelder and Gonzalo Miguez-Macho graciously provided the source code used in Fan et al. (2013) and spent time explaining the concept, code, and required inputs. Gene-Hua Crystal Ng provided helpful advice in assembling and solving the Penman equation. Jed Brown provided advice as to the best way to set up the groundwater flow equation using PETSc. This collaboration resulted from a serendipitous meeting at the Community Surface Dynamics
785   Modeling System (CSDMS) annual meeting, which RB had attended on a CSDMS travel grant.

References

Abatzoglou, J. T., Dobrowski, S. Z., Parks, S. A., and Hegewisch, K. C.: TerraClimate, a high-resolution global dataset of monthly climate and climatic water balance from 1958-2015, Scientific Data, 5, 1–12, https://doi.org/10.1038/sdata.2017.191, 2018.

Amanambu, A. C., Obarein, O. A., Mossa, J., Li, L., Ayeni, S. S., Balogun, O., Oyebamiji, A., and Ochege, F. U.: Groundwater system and climate change: Present status and future considerations, Journal of Hydrology, 589, 125 163, https://doi.org/10.1016/j.jhydrol.2020.125163, 2020.

Amante, C. and Eakins, B. W.: ETOPO1 1 Arc-Minute Global Relief Model: Procedures, Data Sources and Analysis., NOAA Technical Memorandum NESDIS NGDC-24, National Geophysical Data Center, NOAA, https://doi.org/10.7289/V5C8276M, 2009.

Ameli, A. A., McDonnell, J. J., and Bishop, K.: The exponential decline in saturated hydraulic conductivity with depth: a novel method for exploring its effect on water flow paths and transit time distribution, Hydrological Processes, 30, 2438–2450, https://doi.org/10.1002/hyp.10777, 2016.

Anderson, D. G.: Iterative Procedures for Nonlinear Integral Equations, Journal of the ACM (JACM), 12, 547–560, https://doi.org/10.1145/321296.321305, 1965.

Austermann, J., Mitrovica, J. X., Latychev, K., and Milne, G. A.: Barbados-based estimate of ice volume at Last Glacial Maximum affected by subducted plate, Nature Geoscience, 6, 553–557, https://doi.org/10.1038/ngeo1859, 2013.

Austermann, J., Wickert, A. D., Pico, T., Kingslake, J., Callaghan, K. L., and Creel, R. C.: Glacial Isostatic Adjustment Shapes Proglacial Lakes Over Glacial Cycles, Geophysical Research Letters, 49, 1–11, https://doi.org/10.1029/2022GL101191, 2022.

Balay, S., Gropp, W. D., McInnes, L. C., and Smith, B. F.: Efficient Management of Parallelism in Object Oriented Numerical Software Libraries, in: Modern Software Tools in Scientific Computing, edited by Arge, E., Bruaset, A. M., and Langtangen, H. P., pp. 163–202, Birkhäuser Press, 1997.

Balay, S., Abhyankar, S., Adams, M. F., Benson, S., Brown, J., Brune, P., Buschelman, K., Constantinescu, E., Dalcin, L., Dener, A., Eijkhout, V., Faibussowitsch, J., Gropp, W. D., Hapla, V., Isaac, T., Jolivet, P., Karpeev, D., Kaushik, D., Knepley, M. G., Kong, F., Kruger, S., May, D. A., McInnes, L. C., Mills, R. T., Mitchell, L., Munson, T., Roman, J. E., Rupp, K., Sanan, P., Sarich, J., Smith, B. F., Zampini, S., Zhang, H., Zhang, H., and Zhang, J.: PETSc/TAO Users Manual, Tech. Rep. ANL-21/39 - Revision 3.18, Argonne National Laboratory, 2022a.

Balay, S., Abhyankar, S., Adams, M. F., Benson, S., Brown, J., Brune, P., Buschelman, K., Constantinescu, E. M., Dalcin, L., Dener, A., Eijkhout, V., Faibussowitsch, J., Gropp, W. D., Hapla, V., Isaac, T., Jolivet, P., Karpeev, D., Kaushik, D., Knepley, M. G., Kong, F., Kruger, S., May, D. A., McInnes, L. C., Mills, R. T., Mitchell, L., Munson, T., Roman, J. E., Rupp, K., Sanan, P., Sarich, J., Smith, B. F., Zampini, S., Zhang, H., Zhang, H., and Zhang, J.: PETSc Web page, https://petsc.org/, 2022b.

Barnes, R. and Callaghan, K. L.: Depression Hierarchy Source Code, Zenodo, https://doi.org/https://doi.org/10.5281/zenodo.3238558, 2019.

Barnes, R. and Callaghan, K. L.: Fill-Spill-Merge Source Code, Zenodo, https://doi.org/https://doi.org/10.5281/zenodo.3755142, 2020.

Barnes, R., Callaghan, K. L., and Wickert, A. D. A. A. D.: Computing water flow through complex landscapes, Part 2: Finding hierarchies in depressions and morphological segmentations, Earth Surface Dynamics, 8, 431–445, https://doi.org/https://doi.org/10.5194/esurf-2019-34, 2020.

Barnes, R., Callaghan, K., and Wickert, A.: Computing water flow through complex landscapes, Part 3: Fill-Spill-Merge: Flow routing in depression hierarchies, Earth Surface Dynamics, 9, 105–121, https://doi.org/https://doi.org/10.5194/esurf-9-105-2021, 2021.

Callaghan, K. L.: Water Table Model (WTM): Source Code, https://doi.org/10.5281/zenodo.8092449, 2023.

Callaghan, K. L. and Wickert, A. D.: Computing water flow through complex landscapes - Part 1: Incorporating depressions in flow routing using FlowFill, Earth Surface Dynamics, 7, 737–753, https://doi.org/https://doi.org/10.5194/esurf-7-737-2019, 2019.

825 Cardenas, M. B. and Jiang, X. W.: Groundwater flow, transport, and residence times through topography-driven basins with exponentially decreasing permeability and porosity, Water Resources Research, 46, 1–9, https://doi.org/10.1029/2010WR009370, 2010.

Center, N. N. G. D.: ETOPO1 1 Arc-Minute Global Relief Model, 2009.

Charnock, H.: Wind stress on a water surface, Quarterly Journal of the Royal Meteorological Society, 81, 639–640, https://doi.org/10.1002/qj.49708135026, 1955.

830 Clapp, R. B. and Hornberger, G. M.: Empirical equations for some soil hydraulic properties, Water resources research, 14, 1978.

Cuthbert, M. O., Gleeson, T., Moosdorf, N., Befus, K. M., Schneider, A., Hartmann, J., and Lehner, B.: Global patterns and dynamics of climate–groundwater interactions, Nature Climate Change, 9, 137–141, https://doi.org/10.1038/s41558-018-0386-4, 2019a.

Cuthbert, M. O., Taylor, R. G., Favreau, G., Todd, M. C., Shamsudduha, M., Villholth, K. G., MacDonald, A. M., Scanlon, B. R., Kotchoni, D. O., Vouillamoz, J. M., Lawson, F. M., Adjomayi, P. A., Kashaigili, J., Seddon, D., Sorensen, J. P., Ebrahim, G. Y., Owor, M., Nyenje,

835 P. M., Nazoumou, Y., Goni, I., Ousmane, B. I., Sibanda, T., Ascott, M. J., Macdonald, D. M., Agyekum, W., Koussoubé, Y., Wanke, H., Kim, H., Wada, Y., Lo, M. H., Oki, T., and Kukuric, N.: Observed controls on resilience of groundwater to climate variability in sub-Saharan Africa, Nature, 572, 230–234, https://doi.org/10.1038/s41586-019-1441-7, 2019b.

Dalca, A., Ferrier, K., Mitrovica, J., Perron, J., Milne, G., and Creveling, J.: On postglacial sea level - III. Incorporating sediment redistribution, Geophysical Journal International, 194, 45–60, https://doi.org/10.1093/gji/ggt089, 2013.

840 Dean, J. F., Middelburg, J. J., Röckmann, T., Aerts, R., Blauw, L. G., Egger, M., Jetten, M. S. M., de Jong, A. E. E., Meisel, O. H., Rasigraf, O., Slomp, C. P., in't Zandt, M. H., and Dolman, A. J.: Methane Feedbacks to the Global Climate System in a Warmer World, Reviews of Geophysics, 56, 207–250, https://doi.org/10.1002/2017RG000559, 2018.

Decharme, B., Delire, C., Minvielle, M., Colin, J., Vergnes, J. P., Alias, A., Saint-Martin, D., Séférian, R., Sénési, S., and Voldoire, A.: Recent Changes in the ISBA-CTRIP Land Surface System for Use in the CNRM-CM6 Climate Model and in Global Off-Line Hydrological

845 Applications, Journal of Advances in Modeling Earth Systems, 11, 1207–1252, https://doi.org/10.1029/2018MS001545, 2019.

Dingman, L.: Physical hydrology, Macmillan Pub. Co., New York, 1994.

Döll, P., Fiedler, K., and Zhang, J.: Global-scale analysis of river flow alterations due to water withdrawals and reservoirs, Hydrology and Earth System Sciences, 13, 2413–2432, https://doi.org/10.5194/hess-13-2413-2009, 2009.

Döll, P., Trautmann, T., Göllner, M., and Schmied, H. M.: A global-scale analysis of water storage dynamics of inland wetlands: Quan-

850 tifying the impacts of human water use and man-made reservoirs as well as the unavoidable and avoidable impacts of climate change, Ecohydrology, 13, 1–18, https://doi.org/10.1002/eco.2175, 2020.

Dunne, T. and Black, R. D.: An experimental investigation runoff production in permeable soils, Water Resources Research, 6, 478–490, 1970.

Earle, S.: Physical Geology, Victoria, B. C., https://opentextbc.ca/geology/, 2015.

855 European Centre for Medium-Range Weather Forecasts: ERA5 Reanalysis (Monthly Mean 0.25 Degree Latitude-Longitude Grid), https://doi.org/https://doi.org/10.5065/P8GT-0R61, 2019.

Fan, Y. and Miguez-Macho, G.: A simple hydrologic framework for simulating wetlands in climate and earth system models, Climate Dynamics, 37, 253–278, https://doi.org/10.1007/s00382-010-0829-8, 2011.

Fan, Y., Miguez-Macho, G., Weaver, C. P., Walko, R., and Robock, A.: Incorporating water table dynamics in climate modeling:
860   1. Water table observations and equilibrium water table simulations, Journal of Geophysical Research Atmospheres, 112, 1–17,
      https://doi.org/10.1029/2006JD008111, 2007.

Fan, Y., Li, H., and Miguez-Macho, G.: Global patterns of groundwater table depth, Science, 339, 940–943,
      https://doi.org/10.1126/science.1229881, 2013.

Finch, J. and Calver, A.: Methods for the quantification of evaporation from lakes, Report, p. 47, 2008.

865   Freeze, R. A. and Cherry, J. A.: Groundwater, Prentice-Hall, Englewood Cliffs, New Jersey, 1979.

GEBCO Bathymetric Compilation Group: GEBCO_2020 Grid, https://doi.org/doi:10.5285/a29c5465-b138-234d-e053-6c86abc040b9, 2020.

Gleeson, T., Befus, K. M., Jasechko, S., Luijendijk, E., and Cardenas, M. B.: The global volume and distribution of modern groundwater,
      Nature Geoscience, 9, 161–164, https://doi.org/10.1038/ngeo2590, 2016.

Gorbarenko, S. A., Shi, X., Bosin, A. A., Liu, Y., Artemova, A. V., Zou, J., Yanchenko, E. A., Vasilenko, Y. P., Wu, Y., and Vladimirov,
870   A. S.: Relative sea level changes during the Last Glacial Maximum and deglaciation (33–15 ka) inferred from the δ18O records of
      planktic foraminifera from the Sea of Japan, Quaternary Science Reviews, 279, 107 386, https://doi.org/10.1016/j.quascirev.2022.107386,
      2022.

He, F.: Simulating transient climate evolution of the last deglaciation with CCSM3, Ph.D. thesis, University of Wisconsin-Madison, 2011.

Hersbach, H.: Sea surface roughness and drag coefficient as functions of neutral wind speed, Journal of Physical Oceanography, 41, 247–251,
875   https://doi.org/10.1175/2010JPO4567.1, 2011.

Horton, R. E. and Htrata, T.: Erosional development of streams and their drainage basins, hydrophysical approach to quantitative morphology,
      Nihon Ringakkai Shi/Journal of the Japanese Forestry Society, 37, 417–420, https://doi.org/10.11519/jjfs1953.37.9_417, 1955.

Hu, S., Niu, Z., Chen, Y., Li, L., and Zhang, H.: Global wetlands: Potential distribution, wetland loss, and status, Science of the Total
      Environment, 586, 319–327, https://doi.org/10.1016/j.scitotenv.2017.02.001, 2017.

880   Kendall, R. A., Mitrovica, J. X., and Milne, G. A.: On post-glacial sea level – II . Numerical formulation and comparative results on spheri-
      cally symmetric models, Geophysical Journal International, 161, 679–706, https://doi.org/10.1111/j.1365-246X.2005.02553.x, 2005.

Koirala, S., Yeh, P. J., Hirabayashi, Y., Kanae, S., and Oki, T.: Global-scale land surface hydrologic modeling with the representation of water
      table dynamics, Journal of Geophysical Research, 119, 75–89, https://doi.org/10.1002/2013JD020398, 2014.

Kollet, S. J.: Influence of soil heterogeneity on evapotranspiration under shallow water table conditions: Transient, stochastic simulations,
885   Environmental Research Letters, 4, https://doi.org/10.1088/1748-9326/4/3/035007, 2009.

Konikow, L. F.: Contribution of global groundwater depletion since 1900 to sea-level rise, Geophysical Research Letters, 38, 1–5,
      https://doi.org/10.1029/2011GL048604, 2011.

Kourzeneva, E., Asensio, H., Martin, E., and Faroux, S.: Global gridded dataset of lake coverage and lake depth for use
      in numerical weather prediction and climate modelling, Tellus, Series A: Dynamic Meteorology and Oceanography, 64,
890   https://doi.org/10.3402/tellusa.v64i0.15640, 2012.

Lambeck, K., Rouby, H., Purcell, A., Sun, Y., and Sambridge, M.: Sea level and global ice volumes from the Last Glacial Maxi-
      mum to the Holocene, Proceedings of the National Academy of Sciences of the United States of America, 111, 15 296–15 303,
      https://doi.org/10.1073/pnas.1411762111, 2014.

Lawrence, D. M., Fisher, R. A., Koven, C. D., Oleson, K. W., Swenson, S. C., Bonan, G., Collier, N., Ghimire, B., van Kampenhout, L.,
895   Kennedy, D., Kluzek, E., Lawrence, P. J., Li, F., Li, H., Lombardozzi, D., Riley, W. J., Sacks, W. J., Shi, M., Vertenstein, M., Wieder,
      W. R., Xu, C., Ali, A. A., Badger, A. M., Bisht, G., van den Broeke, M., Brunke, M. A., Burns, S. P., Buzan, J., Clark, M., Craig, A.,

Dahlin, K., Drewniak, B., Fisher, J. B., Flanner, M., Fox, A. M., Gentine, P., Hoffman, F., Keppel-Aleks, G., Knox, R., Kumar, S., Lenaerts, J., Leung, L. R., Lipscomb, W. H., Lu, Y., Pandey, A., Pelletier, J. D., Perket, J., Randerson, J. T., Ricciuto, D. M., Sanderson, B. M., Slater, A., Subin, Z. M., Tang, J., Thomas, R. Q., Val Martin, M., and Zeng, X.: The Community Land Model Version 5: Description of New Features, Benchmarking, and Impact of Forcing Uncertainty, Journal of Advances in Modeling Earth Systems, 11, 4245–4287, https://doi.org/10.1029/2018MS001583, 2019.

Lemieux, J. M., Sudicky, E. A., Peltier, W. R., and Tarasov, L.: Dynamics of groundwater recharge and seepage over the Canadian landscape during the Wisconsinian glaciation, Journal of Geophysical Research: Earth Surface, 113, 1–18, https://doi.org/10.1029/2007JF000838, 2008.

Liu, Y. B. and Smedt, F. D.: WetSpa Extension , A GIS-based Hydrologic Model for Flood Prediction and Watershed Management Documentation and User Manual, pp. 1–126, 2004.

Märker, M. and Flörke, M.: Preliminary assessment of IPCC-SRES scenarios on future water resources using the WaterGAP 2 model, International Congress on . . . , pp. 440–445, http://www.mssanz.org.au/MODSIM03/Volume_01/A07/03_Maerker.pdf, 2003.

Maxwell, R. M., Condon, L. E., and Kollet, S. J.: A high-resolution simulation of groundwater and surface water over most of the continental US with the integrated hydrologic model ParFlow v3, Geoscientific Model Development, 8, 923–937, https://doi.org/10.5194/gmd-8-923-2015, 2015.

Messager, M. L., Lehner, B., Grill, G., Nedeva, I., and Schmitt, O.: Estimating the volume and age of water stored in global lakes using a geo-statistical approach, Nature Communications, 7, 1–11, https://doi.org/10.1038/ncomms13603, 2016.

Monteith, J.: Evaporation and environment, Symposia of the Society for Experimental Biology, pp. 205–234, 1965.

Müller Schmied, H., Caceres, D., Eisner, S., Flörke, M., Herbert, C., Niemann, C., Asali Peiris, T., Popat, E., Theodor Portmann, F., Reinecke, R., Schumacher, M., Shadkam, S., Telteu, C. E., Trautmann, T., and Döll, P.: The global water resources and use model WaterGAP v2.2d: Model description and evaluation, Geoscientific Model Development, 14, 1037–1079, https://doi.org/10.5194/gmd-14-1037-2021, 2021.

Neteler, M., Bowman, M. H., Landa, M., and Metz, M.: GRASS GIS: A multi-purpose open source GIS, Environmental Modelling & Software, 31, 124–130, https://doi.org/10.1016/j.envsoft.2011.11.014, 2012.

Ni, S., Chen, J., Wilson, C. R., Li, J., Hu, X., and Fu, R.: Global Terrestrial Water Storage Changes and Connections to ENSO Events, Surveys in Geophysics, 39, 1–22, https://doi.org/10.1007/s10712-017-9421-7, 2018.

NOAA: National Water Model: Improving NOAA's Water Prediction Services, p. 2, http://water.noaa.gov/documents/wrn-national-water-model.pdf, 2016.

Oleson, K., Lawrence, D., Bonan, G., Flanner, M., Kluzek, E., Lawrence, P., Levis, S., Swenson, S., and Thornton, P.: Technical Description of version 4.0 of the Community Land Model (CLM), NCAR Technical Note NCAR/TN-478+STR, p. 257, 2010.

O'Neill, M. M., Tijerina, D. T., Condon, L. E., and Maxwell, R. M.: Assessment of the ParFlow-CLM CONUS 1.0 integrated hydrologic model: evaluation of hyper-resolution water balance components across the contiguous United States, Geoscientific Model Development, 14, 7223–7254, https://doi.org/10.5194/gmd-14-7223-2021, 2021.

Peirce, J. J., Weiner, R. F., and Vesilind, P. A.: Environmental Pollution and Control, Butterworth-Heinemann, fourth ed edn., 1998.

Peltier, W., Argus, D., and Drummond, R.: Space geodesy constrains ice age terminal deglaciation: The global ICE-6G_C (VM5a) model, Journal of Geophysical Research: Solid Earth, 120, 450–487, https://doi.org/10.1002/2014JB011176 Key, 2015.

Penman, H.: Natural evaporation from open water, bare soil and grass, Proceedings of the Royal Society of London. Series A. Mathematical and Physical Sciences, 193, 120–145, 1948.

Pokhrel, Y. N., Hanasaki, N., Yeh, P. J., Yamada, T. J., Kanae, S., and Oki, T.: Model estimates of sea-level change due to anthropogenic impacts on terrestrial water storage, Nature Geoscience, 5, 389–392, https://doi.org/10.1038/ngeo1476, 2012.

Reinecke, R., Foglia, L., Mehl, S., Herman, J. D., Wachholz, A., Trautmann, T., and Döll, P.: Spatially distributed sensitivity of simulated global groundwater heads and flows to hydraulic conductivity, groundwater recharge, and surface water body parameterization, Hydrology and Earth System Sciences, 23, 4561–4582, https://doi.org/10.5194/hess-23-4561-2019, 2019a.

Reinecke, R., Foglia, L., Mehl, S., Trautmann, T., Cáceres, D., and Döll, P.: Challenges in developing a global gradient-based groundwater model (G3M v1.0) for the integration into a global hydrological model, Geoscientific Model Development, 12, 2401–2418, https://doi.org/10.5194/gmd-12-2401-2019, 2019b.

Ringeval, B., De Noblet-Ducoudré, N., Ciais, P., Bousquet, P., Prigent, C., Papa, F., and Rossow, W. B.: An attempt to quantify the impact of changes in wetland extent on methane emissions on the seasonal and interannual time scales, Global Biogeochemical Cycles, 24, 1–12, https://doi.org/10.1029/2008GB003354, 2010.

Sousa, M. R., Jones, J. P., Frind, E. O., and Rudolph, D. L.: A simple method to assess unsaturated zone time lag in the travel time from ground surface to receptor, Journal of Contaminant Hydrology, 144, 138–151, https://doi.org/10.1016/j.jconhyd.2012.10.007, 2013.

Sun, J., Wang, L., Peng, Z., Fu, Z., and Chen, C.: The Sea Level Fingerprints of Global Terrestrial Water Storage Changes Detected by GRACE and GRACE-FO Data, Pure and Applied Geophysics, 179, 3493–3509, https://doi.org/10.1007/s00024-022-03123-8, 2022.

Syed, T. H., Famiglietti, J. S., Rodell, M., Chen, J., and Wilson, C. R.: Analysis of terrestrial water storage changes from GRACE and GLDAS, Water Resources Research, 44, https://doi.org/10.1029/2006WR005779, 2008.

Tarboton, D.: Great Salt Lake Bathymetry, HydroShare, http://www.hydroshare.org/resource/582060f00f6b443bb26e896426d9f62a, 2017.

Valiantzas, J. D.: Simplified versions for the Penman evaporation equation using routine weather data, Journal of Hydrology, 331, 690–702, https://doi.org/10.1016/j.jhydrol.2006.06.012, 2006.

Verpoorter, C., Kutser, T., Seekell, D. A., and Tranvik, L. J.: A global inventory of lakes based on high-resolution satellite imagery, Geophysical Research Letters, 41, 6396–6402, https://doi.org/10.1002/2014GL060641, 2014.

Virtanen, P., Gommers, R., Oliphant, T. E., Haberland, M., Reddy, T., Cournapeau, D., Burovski, E., Peterson, P., Weckesser, W., Bright, J., van der Walt, S. J., Brett, M., Wilson, J., Millman, J. K., Mayorov, N., Nelson, A. R., Jones, E., Kern, R., Larson, E., Carey, C., Polat, L., Feng, Y., Moore, E. W., Van der Plas, J., Laxalde, D., Perktold, J., Cimrman, R., Henriksen, I., Quintero, E., Harris, C. R., Archibald, A. M., Ribeiro, A. H., Pedregosa, F., van Mulbregt, P., and Contributors: SciPy 1.0: Fundamental Algorithms for Scientific Computing in Python, Nature Methods, 2020.

Vörösmarty, C. J., Federer, C. A., and Schloss, A. L.: Potential evaporation functions compared on US watersheds: Possible implications for global-scale water balance and terrestrial ecosystem modeling, Journal of Hydrology, 207, 147–169, https://doi.org/10.1016/S0022-1694(98)00109-7, 1998.

Wada, Y.: Modeling Groundwater Depletion at Regional and Global Scales: Present State and Future Prospects, Surveys in Geophysics, 37, 419–451, https://doi.org/10.1007/s10712-015-9347-x, 2016.

Wada, Y., Van Beek, L. P., Sperna Weiland, F. C., Chao, B. F., Wu, Y. H., and Bierkens, M. F.: Past and future contribution of global groundwater depletion to sea-level rise, Geophysical Research Letters, 39, 1–6, https://doi.org/10.1029/2012GL051230, 2012.

Wickert, A. D.: Potential open water evaporation from TerraClimate, Zenodo, https://doi.org/https://doi.org/10.5281/zenodo.4391500, 2020.

Wickert, A. D., Mitrovica, J. X., Williams, C., and Anderson, R. S.: Gradual demise of a thin southern Laurentide ice sheet recorded by Mississippi drainage, Nature, 502, 668–671, https://doi.org/10.1038/nature12609, 2013.

Wiltshire, A. J., Carolina Duran Rojas, M., Edwards, J. M., Gedney, N., Harper, A. B., Hartley, A. J., Hendry, M. A., Robertson, E., and Smout-Day, K.: JULES-GL7: The Global Land configuration of the Joint UK Land Environment Simulator version 7.0 and 7.2, Geoscientific Model Development, 13, 483–505, https://doi.org/10.5194/gmd-13-483-2020, 2020.

Yokohata, T., Kinoshita, T., Sakurai, G., Pokhrel, Y., Ito, A., Okada, M., Satoh, Y., Kato, E., Nitta, T., Fujimori, S., Felfelani, F., Masaki, Y., Iizumi, T., Nishimori, M., Hanasaki, N., Takahashi, K., Yamagata, Y., and Emori, S.: MIROC-INTEG-LAND version 1: A global biogeochemical land surface model with human water management, crop growth, and land-use change, Geoscientific Model Development, 13, 4713–4747, https://doi.org/10.5194/gmd-13-4713-2020, 2020.

Zeng, X., Shajkh, M., Dai, Y., Dickinson, R. E., and Myneni, R.: Coupling of the Common Land Model to the NCAR Community Climate Model, Journal of Climate, 15, 1832–1854, https://doi.org/10.1175/1520-0442(2002)015<1832:COTCLM>2.0.CO;2, 2002.

Zhang, X., Liu, L., Zhao, T., Chen, X., Lin, S., Wang, J., Mi, J., and Liu, W.: GWL-FCS30: a global 30m wetland map with a fine classification system using multi-sourced and time-series remote sensing imagery in 2020, Earth System Science Data, 15, 265–293, https://doi.org/10.5194/essd-15-265-2023, 2023a.

Zhang, Z., Poulter, B., Feldman, A. F., Ying, Q., Ciais, P., Peng, S., and Li, X.: Recent intensification of wetland methane feedback, Nature Climate Change, 13, 430–433, https://doi.org/10.1038/s41558-023-01629-0, 2023b.

Zhu, P. and Gong, P.: Suitability mapping of global wetland areas and validation with remotely sensed data, Science China Earth Sciences, 57, 2283–2292, https://doi.org/10.1007/s11430-014-4925-1, 2014.

Zotarelli, L. and Dukes, M.: Step by step calculation of the Penman-Monteith Evapotranspiration (FAO-56 Method), Institute of Food and Agricultural Sciences, pp. 1–10, https://edis.ifas.ufl.edu/pdffiles/AE/AE45900.pdf, 2010.